

# Long-term optical, UV, and X-ray continuum variations in the changing-look AGN HE 1136-2304

M. Zetzl<sup>1</sup>, W. Kollatschny<sup>1</sup>, M. W. Oechmann<sup>1</sup>, D. Grupe<sup>2</sup>, M. Haas<sup>3</sup>, M. Ramolla<sup>3</sup>, D. Chelouche<sup>4</sup>, S. Kaspi<sup>5</sup>, N. Schartel<sup>6</sup>

<sup>1</sup> Institut für Astrophysik, Universität Göttingen, Friedrich-Hund Platz 1, D-37077 Göttingen, Germany  
e-mail: wkollat@astro.physik.uni-goettingen.de

<sup>2</sup> Department of Earth and Space Sciences, Morehead State University, Morehead, KY 40351, USA

<sup>3</sup> Astronomisches Institut, Ruhr-Universität Bochum, Universitätsstrasse 150, 44801 Bochum, Germany

<sup>4</sup> Physics Department and the Haifa Research Center for Theoretical Physics and Astrophysics, University of Haifa, Haifa 3498838, Israel

<sup>5</sup> School of Physics & Astronomy and the Wise Observatory, The Raymond and Beverly Sackler Faculty of Exact Sciences Tel-Aviv University, Tel-Aviv 69978, Israel

<sup>6</sup> XMM-Newton Science Operations Centre, ESA, Villafranca del Casuntilo, Apartado 78, 28691 Villanueva de la Cañada, Spain

Received 20 December 2017; Accepted 6 April 2018

## ABSTRACT

**Aims.** A strong outburst in the X-ray continuum and a change of its Seyfert spectral type was detected in HE 1136-2304 in 2014. The spectral type changed from nearly Seyfert 2 type (1.95) to Seyfert 1.5 type in comparison to previous observations taken ten to twenty years before. In a subsequent variability campaign we wanted to investigate whether this outburst was a single event or whether the variability pattern following the outburst was similar to those seen in other variable Seyfert galaxies.

**Methods.** In addition to a SALT spectral variability campaign, we carried out optical continuum as well as X-ray and UV (*Swift*) monitoring studies from 2014 to 2017.

**Results.** HE 1136-2304 strongly varied on timescales of days to months from 2014 to 2017. No systematic trends were found in the variability behavior following the outburst in 2014. A general decrease in flux would have been expected for a tidal disruption event. This could not be confirmed. More likely the flux variations are connected to irregular fluctuations in the accretion rate. The strongest variability amplitudes have been found in the X-ray regime: HE 1136-2304 varied by a factor of eight during 2015. The amplitudes of the continuum variability (from the UV to the optical) systematically decreased with wavelength following a power law  $F_{\text{var}} = a \cdot \lambda^{-c}$  with  $c = 0.84$ . There is a trend that the B-band continuum shows a delay of three light days with respect to the variable X-ray flux. The Seyfert type 1.5 did not change despite the strong continuum variations for the period between 2014 and 2017.

**Key words.** Galaxies: active – Galaxies: Seyfert – Galaxies: nuclei – Galaxies: individual: HE 1136-2304 – (Galaxies:) quasars: emission lines

## 1. Introduction

It is generally known that Seyfert 1 galaxies are variable in the optical and in X-rays on timescales of days to decades. Several active galactic nuclei (AGN) have shown variations in the X-ray continuum by a factor of more than 20 (e.g., Grupe et al. 2001, 2010). AGN that show extreme X-ray flux variations in combination with X-ray spectral variations, i.e., when a Compton-thick AGN becomes Compton-thin and vice versa, were designated as changing-look AGN (e.g., Guainazzi 2002). By analogy, optical changing-look AGN exhibit transitions from type 1 to type 2 and vice versa. In this case, the optical spectral classification can change due to a variation in the intrinsic nuclear power/accretion power, a variation in reddening, or a combination of the two. Typical transition timescales are months to years.

To date about a dozen Seyfert galaxies are known to have changed their optical spectral type, for example, NGC 3515 (Collin-Souffrin et al. 1973), NGC 4151 (Penston & Perez 1984), Fairall 9 (Kollatschny et al. 1985), NGC 2617 (Shappee et al. 2014), Mrk 590 (Denney et al. 2014) and references therein. Further recent findings are based on spectral variations detected by

means of the Sloan Digital Sky Survey (SDSS) (e.g., Komossa et al. 2008, LaMassa et al. 2015, Runnoe et al. 2016, MacLeod et al. 2016). In most of these recent findings only a few optical spectra of the individual SDSS galaxies have been secured to prove their changing-look character.

HE 1136-2304 ( $\alpha_{2000} = 11\text{h } 38\text{m } 51.1\text{s}$ ,  $\delta = -23^\circ 21' 36''$ ) has been detected as a variable X-ray source by the XMM-Newton slew survey in 2014 (Parker et al. 2016). The 0.2–2 keV flux increased by a factor of about 30 in comparison to the ROSAT all-sky survey in 1990. However, no clear evidence of X-ray absorption variability has been seen. HE 1136-2304 changed its optical spectral classification from 1994 (Seyfert 2/1.95) to 2014 (Seyfert 1.5) and can be considered an optical changing-look AGN.

We decided to study the variability behavior of HE 1136-2304 subsequent to its X-ray outburst in 2014 in detail. We carried out optical photometric and spectroscopic variability follow-up studies in combination with *Swift* UV and X-ray photometric observations to investigate the variability behavior of this changing-look galaxy on timescales of weeks to years. The

**Table 1.** Log of spectroscopic observations of HE1136 with SALT. Listed are the Julian date, the UT date, and the exposure time.

Julian Date 2 400 000+	UT Date	Exp. time [s]
56846.248	2014-07-07	1200
57016.559	2014-12-25	985
57070.399	2015-02-16	985
57082.362	2015-02-28	985
57088.594	2015-03-07	985
57100.539	2015-03-19	985
57112.285	2015-03-30	985
57121.256	2015-04-08	985
57131.243	2015-04-18	1230
57167.359	2015-05-24	1144
57171.364	2015-05-28	1144
57182.330	2015-06-08	1144
57187.319	2015-06-13	1144
57192.308	2015-06-18	1144
57196.295	2015-06-22	1144
57201.271	2015-06-27	1144
57206.265	2015-07-02	1144
57217.227	2015-07-13	1144
57399.510	2016-01-12	1200
57519.391	2016-05-10	1196
57540.351	2016-05-31	1196
57889.381	2017-05-15	1218

outburst in HE 1136-2304 could have been caused by a tidal disruption event, by a less drastic variation in the intrinsic nuclear power/accretion power, or by significant variation in the absorption. Although detailed and long-term optical variability studies exist for many AGN, for example NGC 5548 (Peterson et al. 2002, Pei et al. 2017), NGC 7603 (Kollatschny et al. 2000), and 3C 390.3 (Shapovalova et al. 2010), no detailed follow-up studies have been reported for the changing-look-type AGN mentioned above.

This is the first paper in a series. We will discuss the spectral variations seen in 2015 and the broad-line region structure in HE 1136-2304 in a second paper in detail.

Throughout this paper, we assume that  $H_0 = 70 \text{ km s}^{-1} \text{ Mpc}^{-1}$  with a  $\Lambda$ CDM cosmology with  $\Omega_\Lambda=0.73$  and  $\Omega_M=0.27$ . With a redshift of  $z=0.0271$  this results in a luminosity distance of  $D_L = 118 \text{ Mpc}$  using the Cosmology Calculator developed by Wright (2006).

## 2. Observations and data reduction

### 2.1. Optical spectroscopy with the SALT telescope

We took a first optical spectrum of the Seyfert nucleus in HE 1136-2304 with the 10 m Southern African Large Telescope (SALT) nearly simultaneously with X-ray observations by XMM-Newton on 2014 July 07, just after the X-ray flaring (Parker et al. 2016). To study the subsequent variability behavior, we took additional optical spectra at 17 epochs with the SALT telescope between 2014 December 25 and 2015 July 13. To examine the long-term trend, four additional spectra were taken: three spectra in 2016 between January 12 and May 31 and one spectrum in 2017 on May 15. The log of our spectroscopic observations with SALT is given in Table 1. The Julian dates in all tables mark the beginning of the observations. We acquired 16 spectra between 2015 February and 2015 July with a mean interval of 9 days. The spacing of our observations was not regular.

The shortest time interval between two subsequent observations was four days.

All spectroscopic observations were taken under identical instrumental conditions with the Robert Stobie Spectrograph attached to the SALT telescope using the PG0900 grating. The slit width was fixed to  $2''.0$  projected onto the sky at an optimized position angle to minimize differential refraction. Furthermore, all observations were taken at the same air mass thanks to the particular design feature of the SALT. All spectra were taken with exposure times of 10 to 20 minutes (see Table 1). Typical seeing full width at half maximum (FWHM) values were 1 to 2 arcsec.

We covered the wavelength range from 4355 to 7230 Å at a spectral resolution of 6.5 Å. The observed wavelength range corresponds to a wavelength range from 4240 to 7040 Å in the rest frame of the galaxy. There are two gaps in the spectrum caused by the gaps between the three CCDs: one between the blue and the central CCD chip, and one between the central and red CCD chip covering the wavelength ranges 5206–5263 Å and 6254–6309 Å (5069–5124 Å and 6089–6142 Å in the rest frame). All spectra were wavelength corrected to the rest frame of the galaxy ( $z=0.0271$ ).

In addition to the galaxy spectra, we also observed necessary flat-field and Xe arc frames, as well as spectrophotometric standard stars for flux calibration (EG274, LTT3218, LTT7379). The spatial resolution per binned pixel was  $0''.2534$  for our SALT spectra. We extracted eight columns from our object spectrum corresponding to  $2''.03$ . The reduction of the spectra (bias subtraction, cosmic ray correction, flat-field correction, 2D wavelength calibration, night sky subtraction, and flux calibration) was done in a homogeneous way with IRAF reduction packages (e.g., Kollatschny et al. 2001). We obtained typical S/N values of 40 in the continua of the galaxy spectra.

Great care was taken to ensure high-quality intensity and wavelength calibrations to keep the intrinsic measurement errors very low, as described in Kollatschny et al. (2001, 2003, 2010). Our AGN spectra and our calibration star spectra were not always taken under photometric conditions. Therefore, all spectra were calibrated to the same absolute [O III]  $\lambda 5007$  flux of  $1.75 \times 10^{-13} \text{ erg s}^{-1} \text{ cm}^{-2}$  (Reimers et al. 1996). The flux of the narrow emission line [O III]  $\lambda 5007$  is considered to be constant on timescales of many years. A relative flux accuracy on the order of 1% was achieved for most of our spectra.

### 2.2. Optical, UV, and X-ray observations with Swift

After the discovery of the X-ray flaring in June 2014 (Parker et al. 2016), we started monitoring HE 1136-2304 with *Swift* (Gehrels et al. 2004) in X-rays and the UV/optical. All *Swift* observing dates and exposure times are listed in Table A.1. In this paper, we focus on the *Swift* observations between 2014 June 06 and 2016 February 02. However, HE 1136-2304 had been observed previously by *Swift* during three epochs in 2010. For comparison purposes, we list these observations in all the tables relevant to *Swift* data (see Tables 2, 3, and A.1).

Most X-ray observations with the *Swift* X-ray Telescope (XRT, Burrows et al. 2005) were performed in photon counting mode (pc-mode, Hill et al. 2004). However, the four observations in 2014 August were performed in windowed timing mode. For the pc-mode data, source counts were collected in a circular region with a radius of 30 pixels (equivalent to  $70''$ ) and background counts in a nearby source-free circular region with a radius of 90 pixels (equal to  $210''$ ). The windowed timing source and background spectra were selected in

**Table 2.** *Swift* monitoring: V, B, U, UVOT W1, M2, and W2 observed flux densities in units of  $10^{-15} \text{ erg s}^{-1} \text{ cm}^{-2} \text{ \AA}^{-1}$  (columns 2 to 7) and magnitudes in the Vega system (columns 8 to 13).

JD-2400000	V	B	U	UVW1	UVM2	UVW2	V	B	U	UV W1	UV M2	UVW2
(1)	(2)	(3)	(4)	(5)	(6)	(7)	(8)	(9)	(10)	(11)	(12)	(13)
55350.7604					1.12 ± 0.04						16.23±0.06	
55420.4688				1.00 ± 0.06						16.27±0.06		
55424.4167				0.93 ± 0.05						16.35±0.06		
56833.6090	2.64 ± 0.11	2.35 ± 0.09	2.49 ± 0.12	1.92 ± 0.13	1.84 ± 0.09	1.83 ± 0.10	15.38±0.05	15.96±0.06	15.20±0.06	15.56±0.07	15.69±0.08	15.89±0.07
56840.3437						1.77 ± 0.07						15.78±0.06
56844.1424	2.46 ± 0.13	2.20 ± 0.10	2.35 ± 0.13	1.81 ± 0.14	1.70 ± 0.10	1.55 ± 0.09	15.35±0.06	16.04±0.06	15.26±0.06	15.63±0.08	15.77±0.09	16.08±0.07
56847.2729					1.56 ± 0.06						15.86±0.07	
56850.9375					1.61 ± 0.06						15.83±0.06	
56854.8646					1.77 ± 0.07						15.72±0.07	
56861.9479					2.14 ± 0.07						15.51±0.07	
56862.6007					2.21 ± 0.08						15.49±0.06	
56866.9965					2.11 ± 0.07						15.54±0.06	
56871.0729					2.22 ± 0.08						15.48±0.06	
56874.1007					2.06 ± 0.07						15.56±0.06	
56878.5347					1.88 ± 0.08						15.66±0.07	
56882.7340					1.67 ± 0.06						15.79±0.06	
57085.3507			2.02 ± 0.08						15.43±0.05			
57087.5208				1.73 ± 0.10						15.67±0.03		
57132.3125	2.30 ± 0.11	1.94 ± 0.08	1.77 ± 0.10	1.44 ± 0.11	1.34 ± 0.08	1.34 ± 0.09	15.42±0.06	16.17±0.06	15.57±0.06	15.87±0.08	16.03±0.09	16.24±0.08
57138.7500	2.12 ± 0.09	1.69 ± 0.07	1.60 ± 0.08	1.13 ± 0.08	1.09 ± 0.06	1.03 ± 0.06	15.50±0.05	16.32±0.06	15.68±0.06	16.13±0.08	16.25±0.08	16.52±0.07
57145.8368	2.20 ± 0.11	1.75 ± 0.08	1.60 ± 0.09	1.20 ± 0.10	1.05 ± 0.07	1.10 ± 0.07	15.46±0.06	16.28±0.06	15.68±0.06	16.07±0.08	16.29±0.09	16.45±0.08
57152.6875	2.13 ± 0.09	1.65 ± 0.06	1.32 ± 0.07	0.98 ± 0.07	1.01 ± 0.11	0.87 ± 0.05	15.50±0.05	16.34±0.05	15.89±0.06	16.30±0.08	16.33±0.14	16.70±0.07
57160.9028	2.12 ± 0.14	1.59 ± 0.09	1.45 ± 0.10	1.16 ± 0.12	0.88 ± 0.10	0.92 ± 0.08	15.51±0.08	16.39±0.08	15.79±0.08	16.11±0.10	16.48±0.14	16.65±0.10
57167.0833	2.09 ± 0.09	1.76 ± 0.07	1.57 ± 0.08	1.27 ± 0.09	1.02 ± 0.06	1.07 ± 0.06	15.53±0.05	16.28±0.05	15.70±0.06	16.01±0.07	16.33±0.08	16.48±0.07
57173.8160	2.05 ± 0.10	1.74 ± 0.08	1.39 ± 0.08	0.97 ± 0.08	0.90 ± 0.06	0.91 ± 0.06	15.56±0.06	16.29±0.06	15.83±0.07	16.30±0.09	16.57±0.10	16.66±0.08
57181.0000	1.97 ± 0.08	1.53 ± 0.06	1.19 ± 0.06	0.87 ± 0.06	0.67 ± 0.04	0.71 ± 0.04	15.59±0.05	16.43±0.05	16.00±0.06	16.42±0.08	16.78±0.09	16.88±0.07
57187.8056	2.01 ± 0.09	1.43 ± 0.06	1.09 ± 0.07	0.71 ± 0.06	0.60 ± 0.04	0.67 ± 0.04	15.56±0.05	16.50±0.06	16.09±0.07	16.63±0.09	16.89±0.10	16.98±0.08
57194.9236	1.98 ± 0.09	1.47 ± 0.07	1.05 ± 0.07	0.77 ± 0.06	0.60 ± 0.04	0.66 ± 0.04	15.58±0.05	16.47±0.06	16.14±0.07	16.56±0.09	16.90±0.10	17.00±0.08
57201.8785	1.95 ± 0.10	1.49 ± 0.07	1.18 ± 0.07	0.83 ± 0.07	0.77 ± 0.05	0.75 ± 0.05	15.60±0.06	16.46±0.06	16.01±0.07	16.48±0.09	16.63±0.10	16.86±0.08
57209.3986	2.06 ± 0.09	1.66 ± 0.06	1.32 ± 0.07	0.91 ± 0.07	0.79 ± 0.04	0.86 ± 0.05	15.54±0.05	16.34±0.06	15.89±0.06	16.38±0.08	16.60±0.08	16.71±0.07
57218.2188	1.88 ± 0.09	1.59 ± 0.07	1.34 ± 0.07	0.96 ± 0.07	0.78 ± 0.05	0.73 ± 0.05	15.64±0.05	16.48±0.06	15.87±0.06	16.31±0.08	16.62±0.09	16.90±0.08
57222.6285	1.98 ± 0.09	1.51 ± 0.06	1.21 ± 0.07	0.94 ± 0.07	0.82 ± 0.05	0.79 ± 0.05	15.58±0.05	16.44±0.06	15.98±0.06	16.33±0.08	16.56±0.09	16.81±0.07
57229.9167	2.03 ± 0.09	1.56 ± 0.07	1.25 ± 0.07	0.89 ± 0.07	0.69 ± 0.04	0.77 ± 0.05	15.55±0.05	16.40±0.06	15.95±0.06	16.39±0.08	16.65±0.09	16.73±0.08
57236.9687	2.09 ± 0.09	1.58 ± 0.07	1.28 ± 0.07	0.90 ± 0.07	0.86 ± 0.05	0.87 ± 0.06	15.52±0.05	16.39±0.06	15.92±0.06	16.39±0.08	16.51±0.09	16.70±0.07
57337.5763	2.13 ± 0.10	1.95 ± 0.08	1.79 ± 0.09	1.44 ± 0.10	1.23 ± 0.07	1.29 ± 0.08	15.51±0.05	16.17±0.06	15.56±0.06	15.88±0.07	16.11±0.08	16.28±0.07
57421.3507	2.34 ± 0.10	2.00 ± 0.07	1.88 ± 0.09	1.41 ± 0.09	1.23 ± 0.07	1.24 ± 0.07	15.40±0.05	16.13±0.05	15.50±0.06	15.90±0.07	16.12±0.08	16.32±0.07

**Table 3.** *Swift* monitoring: Julian date, UT date, XRT 0.3–10 keV count rates (CR) and hardness ratios (HR<sup>1</sup>), X-ray photon index  $\Gamma$ , the observed 0.3–10 keV X-ray flux in units of  $10^{-11}$  erg s<sup>-1</sup> cm<sup>-2</sup>, reduced  $\chi^2$  of the simple power-law model fit (pl), X-ray photon index  $\Gamma$  for an intrinsic absorber, and reduced  $\chi^2$  for an intrinsic absorbed power-law model fit (zwa \* pl) of HE 1136-2304.

Julian Date 2 400 000+	UT Date	CR	HR	$\Gamma_{\text{pl}}$	XRT flux	$(\chi^2/\nu)_{\text{pl}}$	$\Gamma_{\text{zwa*pl}}$	$N_{\text{H,intr}}^2$	$(\chi^2/\nu)_{\text{zwa*pl}}$
55350.7604	2010-06-02	0.35±0.01	0.57±0.02	1.55±0.08	1.40 ± 0.06	38.2/42	1.79±0.16	1.04±0.58	28.8/41
55420.4688	2010-08-11	0.24±0.01	0.44±0.06	1.54±0.16	1.19 ± 0.07	10.1/14	—	0 <sup>3</sup>	—
55424.4167	2010-08-15	0.17±0.01	0.63±0.03	1.41±0.12	1.00 ± 0.05	21.1/24	1.58±0.24	0.84±0.84	19.0/23
56833.6090	2014-06-24	0.46±0.02	0.53±0.04	1.58±0.10	1.87 ± 0.10	48.7/26	1.94±0.23	1.31±0.73	39.3/25
56840.3437	2014-07-01	0.47±0.03	0.55±0.04	1.49±0.13	2.30 ± 0.16	27.4/18	1.84±0.27	1.56±1.09	21.5/17
56844.1424	2014-07-05	0.46±0.03	0.61±0.03	1.37±0.12	2.25 ± 0.14	20.7/18	1.68±0.26	1.46±1.05	15.2/17
56847.2729	2014-07-08	0.38±0.02	0.51±0.05	1.61±0.16	1.70 ± 0.15	5.8/13	—	0 <sup>3</sup>	—
56850.9375	2014-07-11	0.45±0.03	0.64±0.04	1.51±0.16	2.12 ± 0.24	20.0/12	2.17±0.40	3.40±1.85	10.0/11
56854.8646	2014-07-15	0.35±0.02	0.44±0.03	1.44±0.20	1.65 ± 0.15	12.1/9	—	0 <sup>3</sup>	—
56861.9479	2014-07-22	0.61±0.03	0.57±0.03	1.43±0.11	2.64 ± 0.16	30.4/23	1.63±0.22	0.89±0.81	27.0/22
56862.6007	2014-07-23	0.43±0.03	0.52±0.05	1.78±0.24	1.94 ± 0.16	6.5/8	—	0 <sup>3</sup>	—
56866.9965	2014-07-27	0.71±0.04	0.55±0.05	1.53±0.11	2.96 ± 0.17	36.7/24	2.04±0.24	1.95±0.83	19.1/23
56871.0729	2014-08-01	0.70±0.04	0.40±0.05 <sup>4</sup>	1.61±0.11	3.02 ± 0.20	37.8/27	2.06±0.25	1.45±0.70	24.0/26
56874.1007	2014-08-04	0.36±0.04	0.40±0.05 <sup>4</sup>	1.56±0.11	2.61 ± 0.14	30.1/26	1.97±0.23	1.34±0.65	16.72/25
56878.5347	2014-08-08	0.39±0.03	0.54±0.07 <sup>4</sup>	1.48±0.17	2.09 ± 0.25	14.8/14	1.84±0.34	1.51±1.25	10.5/13
56882.7340	2014-08-12	0.37±0.04	0.62±0.10 <sup>4</sup>	1.27±0.23	3.53 ± 0.50	11.2/15	—	0 <sup>3</sup>	—
57085.3507	2015-03-03	0.49±0.03	0.51±0.04	1.51±0.15	2.35 ± 0.20	19.2/17	—	0 <sup>3</sup>	—
57087.5208	2015-03-05	0.74±0.04	0.53±0.04	1.46±0.16	3.75 ± 0.29	15.4/13	1.90±0.34	2.12±1.48	9.6/12
57132.3125	2015-04-19	0.28±0.02	0.52±0.05	1.67±0.19	1.18 ± 0.10	13.9/11	1.80±0.28	0.68±0.64	13.5/10
57138.7500	2015-04-25	0.17±0.01	0.56±0.04	1.64±0.17	0.78 ± 0.07	13.7/11	1.87±0.35	1.45±1.45	12.2/13
57145.8368	2015-05-02	0.32±0.02	0.53±0.05	1.44±0.17	1.56 ± 0.14	15.2/14	1.48±0.18	0.21±0.21	15.2/13
57152.6875	2015-05-09	0.10±0.01	0.55±0.06	1.45±0.25	0.48 ± 0.10	1.0/6	—	0 <sup>3</sup>	—
57160.9028	2015-05-17	0.30±0.03	0.57±0.06	1.29±0.19	1.71 ± 0.15	93.6/130 <sup>5</sup>	—	0 <sup>3</sup>	—
57167.0833	2015-05-24	0.42±0.02	0.57±0.03	1.47±0.08	2.07 ± 0.10	54.4/36	1.85±0.17	1.46±0.57	33.3/35
57173.8160	2015-05-30	0.24±0.01	0.60±0.05	1.34±0.17	1.33 ± 0.12	7.1/11	1.80±0.39	2.38±1.80	2.1/10
57181.0000	2015-06-07	0.16±0.01	0.65±0.04	1.51±0.13	0.77 ± 0.05	26.1/16	2.12±0.29	3.61±1.56	8.9/15
57187.8056	2015-06-13	0.09±0.01	0.56±0.06	1.59±0.20	0.48 ± 0.05	118/119 <sup>5</sup>	2.06±0.38	1.89±1.28	112/118 <sup>5</sup>
57194.9236	2015-06-21	0.13±0.01	0.52±0.06	1.36±0.18	0.61 ± 0.08	137/142 <sup>5</sup>	—	0 <sup>3</sup>	—
57201.8785	2015-06-27	0.15±0.01	0.59±0.05	1.52±0.25	0.75 ± 0.11	8.5/7	—	0 <sup>3</sup>	—
57209.3986	2015-07-05	0.16±0.01	0.56±0.05	1.54±0.19	0.76 ± 0.07	12.5/14	—	0 <sup>3</sup>	—
57218.2188	2015-07-14	0.21±0.01	0.64±0.04	1.57±0.15	1.02 ± 0.10	13.9/16	1.89±0.30	1.95±1.58	9.7/15
57222.6285	2015-07-18	0.15±0.01	0.67±0.05	1.33±0.19	0.83 ± 0.12	14.9/10	1.80±0.44	3.41±2.88	11.0/9
57229.9167	2015-07-25	0.16±0.01	0.65±0.05	1.21±0.15	0.86 ± 0.10	16.9/11	1.57±0.31	2.44±1.88	12.0/10
57236.9687	2015-08-01	0.15±0.01	0.60±0.05	1.52±0.18	0.69 ± 0.05	16.5/10	—	0 <sup>3</sup>	—
57337.5763	2015-11-10	0.37±0.02	0.57±0.04	1.52±0.11	1.72 ± 0.09	25.1/27	1.74±0.20	1.07±0.83	20.4/26
57421.3507	2016-02-02	0.25±0.01	0.29±0.03	1.47±0.12	1.33 ± 0.08	21.1/18	1.73±0.21	1.22±0.85	15.3/17

<sup>1</sup> The hardness ratio is defined as  $\text{HR} = \frac{\text{hard}-\text{soft}}{\text{hard}+\text{soft}}$  where *soft* and *hard* are the background corrected counts in the 0.3–1.0 keV and 1.0–10.0 keV bands, respectively

<sup>2</sup> The intrinsic  $N_{\text{H,intr}}$  is given in units of  $10^{21}$  cm<sup>-2</sup>

<sup>3</sup> No additional absorber required. The fit is consistent with Galactic absorption alone.

<sup>4</sup> These observations were performed in windowed timing mode.

<sup>5</sup> Fit using Cash Statistics (Cash 1979)

boxes with a width of 40 pixels each. Spectra were extracted with the *FTOOL XSELECT*. An auxiliary response file (ARF) was created for each observation using *xrtmkarf*. We applied the *Swift* XRT response file *swxpc0to12s6\_20130101v014.rmf* and *swxwt0to2s6\_20131212v015.rmf* for the pc and WT data, respectively. Most spectra were rebinned to have at least 20 counts per bin using *grppha*. For some spectra the number of counts was too low to allow  $\chi^2$  statistics. These data were fitted by Cash statistics (Cash 1979). The spectral analysis was performed in *XSPEC* (Arnaud 1996).

We fitted the X-ray spectra first with a simple power-law model with the absorption parameter fixed to the Galactic value. In addition, we fitted a power-law model with redshifted intrinsic

absorption (zwa) to the data with the redshift fixed to the redshift of HE 1136-2304. For some spectra we found some evidence of a low intrinsic absorption on the order of  $1 \times 10^{21}$  cm<sup>-2</sup>; however, in most cases the absorption column density of the absorber was consistent with the Galactic value and the fits did not require any additional absorber. Finally, all spectra were fitted with a single power-law model with Galactic absorption ( $N_{\text{H,gal}} = 3.3 \times 10^{20}$  cm<sup>-2</sup>; Kalberla et al. 2005). As indicated in Table 3, we also fitted the data with a redshifted intrinsic absorber model.

Count rates, hardness ratios, and the best fit values obtained are listed in Table 3. The hardness ratio is defined as  $\text{HR} = \text{counts}(0.3-1.0 \text{ keV})/\text{counts}(1.0-10.0 \text{ keV})$ . In order to deter-

mine a background corrected hardness ratio, we applied the program *BEHR* by Park et al. (2006).

During most observations, the *Swift* UV-Optical Telescope (UVOT, Roming et al. 2005) observed in all six photometric filters UVW2 (1928 Å), UVM2 (2246 Å), UVW1 (2600 Å), u (3465 Å), b (4392 Å), and v (5468 Å). Before analyzing the data, all snapshots in one segment were combined with the UVOT tool *uvotimsum*. The flux densities and magnitudes in each filter were determined by the tool *uvotsource* using the count rate conversion and calibration, as described in Poole et al. 2008 and Breeveld et al. 2010. Source counts were extracted in a circle with a radius of 5'' and background counts in a nearby source-free region with a radius of 20''. The UVOT fluxes listed in Table 2 are not corrected for Galactic reddening. The reddening value in the direction of HE 1136-2304 is  $E_{B-V} = 0.03666$ , deduced from the Schlafly & Finkbeiner (2011) re-calibration of the Schlegel et al. (1998) infrared-based dust map. Applying equation 2 in Roming et al. (2009), who used the standard reddening correction curves by Cardelli et al. (1989), we calculated the following magnitude corrections:  $v_{\text{corr}} = 0.110$ ,  $b_{\text{corr}} = 0.143$ ,  $u_{\text{corr}} = 0.180$ ,  $UVW1_{\text{corr}} = 0.226$ ,  $UVM2_{\text{corr}} = 0.324$ ,  $UVW2_{\text{corr}} = 0.270$ . For all *Swift* UVOT magnitudes used in this publication we adopted the Vega magnitude system.

### 2.3. Optical photometry with the MONET North and South telescopes

Additional optical B-, V-, and R-band photometric data were collected with the 1.2m MONET/North telescope between 2014 November 17 and 2015 February 04 and with the twin MONET/South telescope between 2016 April 25 and June 21. Table A.2 lists the Julian dates of the MONET observations. The MONET/North and South telescopes are located at McDonald Observatory in Texas, USA, and Sutherland, South Africa, respectively. The data were obtained with the MONET browser-based remote-observing interface. The photometric data were taken with a SBIG STF-8300M CCD camera at MONET/North and with a Spectral Instruments 1100 CCD camera at MONET/South. Typical exposure times were 60 s and 120 s. The photometry was performed relative to three comparison stars approximately 2.0 arcmin west of HE 1136-2304.

### 2.4. Optical photometry with the Bochum telescopes at Cerro Armazones

Between 2015 April and 2016 July HE1136–2304 was monitored in the B and V bands and in a narrowband filter NB<sub>670</sub> covering the redshifted H $\alpha$  line using the 40 cm Bochum Monitoring Telescope (BMT) of the Universitätssternwarte Bochum near Cerro Armazones, Chile (Ramolla et al. 2013). Per night and broadband filter 15 dithered 60 s exposures with a size of 41.2''  $\times$  27'' were obtained; for the narrowband filter NB<sub>670</sub> we took 25 exposures.

We performed additional B-band monitoring using the 25 cm Berlin Exoplanet Search Telescope-II (BEST-II<sup>1</sup>) with 1.7°  $\times$  1.7° FoV (Kabath et al. 2009), also located at the Universitätssternwarte Bochum. Per night 15 dithered 60 s exposures were obtained. We performed standard data reduction including corrections for bias, dark current, flatfield, astrometry, and astrometric distortion before combining the dithered images, separated by telescope, night, and filter. As in Pozo Nuñez et al. (2015) a 7''/5 diameter aperture was used to extract the pho-

tometry and to create flux-normalized light curves relative to 15 nonvariable stars located in the same images, within 10' around HE1136–2304, and of similar brightness to HE1136–2304. Absolute calibration was performed using standard reference stars from Landolt (2009) observed on the same nights as the AGN. We also corrected for atmospheric (Patat et al. 2011) and Galactic foreground extinction (Schlafly & Finkbeiner 2011).

A list of the photometric observations is given in Table A.3.

## 3. Results

Figure 1 shows the mean spectrum of HE 1136-2304 based on our SALT variability campaign in 2015 together with the *Swift* B- and V-band filter curves; the Bochum B, V, and NB<sub>670</sub> filter curves; and the MONET B, V, and R filter curves. The B-band filter curves are shown in blue, the V-band filter curves are given in green, and the R-band filter curves in red. The fluxes in the filter bands are contaminated by both constant and variable emission line contributions.

### 3.1. Optical, UV, and X-ray continuum variations

First we created optical B- and V-band light curves based on the absolute calibration of the *Swift* data. Then we generated B and V light curves by measuring the continuum flux in the SALT spectra at 4570 Å and 5360 Å in the rest frame. Afterwards we created light curves based on the B- and V-band intensities taken with the MONET telescopes. Additionally, we created light curves based on the B and V photometry observed at Cerro Armazones. We intercalibrated all these light curves to the B- and V-band *Swift* data (Table 4). The fluxes in these light curves are not corrected for Galactic absorption. We applied a multiplicative scale factor and an additional flux adjustment component to put the light curves on the same scale and to correct for differences in the host galaxy contribution. These differences are caused by different aperture sizes and by the different instruments attached to our telescopes. Figures 2 and 3 show the combined B- and V-band continuum light curves of HE 1136-2304 from 2014 to 2016. Overall, there is a good agreement between the light curves from the different telescopes.

Optical and 0.3–10 keV *Swift* light curves are shown in Figure 4 along with the X-ray photon index values and the hardness ratios (see Sect. 2.2). All measurements are listed in Table 3. The X-ray 0.3–10 keV flux and count rate are clearly variable by a factor of about 5. We also checked whether there is any significant variability in the hardness ratio and photon index  $\Gamma$ . The 2015 data may suggest hardening. However, testing whether there is any correlation between the count rate and the hardness ratio and  $\Gamma$ , we only found a weak trend with a Spearman rank order correlation coefficient of -0.30 between the count rate and hardness ratio, but with a probability of 6% that this result is just random. This random result is confirmed when checking the correlation between the count rate and  $\Gamma$ , which results in a Spearman rank order correlation coefficient of  $r_s = 0.06$  with a probability  $P = 0.74$  of a random result. We therefore conclude that there is no obvious connection with the X-ray flux/count rate variability and the variability of the hardness ratio. The distribution of the hardness ratios is almost Gaussian.

<sup>1</sup> <https://www.astro.rub.de/Astrophysik/BESTII.html>

**Table 4.** Julian date, UT date, and B- and V-band fluxes taken with the MONET North/South (MN/MS) and VYSOS 16 (V16) telescopes, and with the *Swift* satellite (SW), as well as corresponding continuum fluxes taken with SALT (S).

Julian Date 2 400 000+	UT Date	Cont. Flux B band, 4570 Å	Julian Date 2 400 000+	UT Date	Cont. Flux V band, 5360 Å	Tel.
49066.500	1993-03-20	1.480 ± 0.089	49066.500	1993-03-20	2.046 ± 0.061	ESO
52410.920	2002-05-16	2.051 ± 0.089	52410.920	2002-05-16	2.130 ± 0.031	6dF
56833.609	2014-06-25	2.350 ± 0.090	56833.609	2014-06-25	2.640 ± 0.110	SW
56844.142	2014-07-05	2.200 ± 0.101	56844.142	2014-07-05	2.460 ± 0.130	SW
56846.248	2014-07-07	2.124 ± 0.013	56846.248	2014-07-07	2.358 ± 0.024	S
56979.010	2014-11-17	1.776 ± 0.023	56979.011	2014-11-17	2.058 ± 0.009	MN
56979.968	2014-11-18	1.763 ± 0.013	56979.969	2014-11-18	2.094 ± 0.008	MN
56981.980	2014-11-20	1.783 ± 0.011	56981.981	2014-11-20	2.113 ± 0.006	MN
56982.971	2014-11-21	1.820 ± 0.011	56982.972	2014-11-21	2.077 ± 0.007	MN
56985.947	2014-11-24	1.653 ± 0.014	56985.948	2014-11-24	2.080 ± 0.008	MN
56986.936	2014-11-25	1.663 ± 0.016	56986.937	2014-11-25	2.041 ± 0.008	MN
56988.945	2014-11-27	1.714 ± 0.009	56988.946	2014-11-27	2.069 ± 0.005	MN
56989.936	2014-11-28	1.725 ± 0.011	56989.937	2014-11-28	2.046 ± 0.006	MN
56991.034	2014-11-29	1.859 ± 0.078	56991.035	2014-11-29	2.132 ± 0.036	MN
56991.987	2014-11-30	1.673 ± 0.009	56991.988	2014-11-30	2.060 ± 0.005	MN
56996.924	2014-12-05	1.507 ± 0.054	56996.925	2014-12-05	2.018 ± 0.019	MN
56999.890	2014-12-08	1.570 ± 0.078	56999.892	2014-12-08	1.937 ± 0.052	MN
57004.007	2014-12-12	1.635 ± 0.019	57004.008	2014-12-12	2.010 ± 0.010	MN
57006.928	2014-12-15	1.732 ± 0.054	57006.929	2014-12-15	1.978 ± 0.021	MN
57008.023	2014-12-16	1.685 ± 0.023	57008.025	2014-12-16	2.061 ± 0.014	MN
57009.928	2014-12-18	1.607 ± 0.009	57009.929	2014-12-18	1.992 ± 0.006	MN
57011.018	2014-12-19	1.631 ± 0.008	57011.019	2014-12-19	2.024 ± 0.005	MN
57016.559	2014-12-25	1.503 ± 0.004	57016.559	2014-12-25	1.961 ± 0.015	S
57027.909	2015-01-05	1.521 ± 0.034	57027.910	2015-01-05	1.966 ± 0.013	MN
57029.911	2015-01-07	1.611 ± 0.030	57029.912	2015-01-07	2.027 ± 0.016	MN
57051.844	2015-01-29	1.499 ± 0.018	57051.845	2015-01-29	1.964 ± 0.009	MN
57056.946	2015-02-03	1.528 ± 0.066	57056.947	2015-02-03	2.217 ± 0.038	MN
57057.827	2015-02-04	1.501 ± 0.035	57057.828	2015-02-04	2.052 ± 0.017	MN
57070.399	2015-02-16	1.600 ± 0.014	57070.399	2015-02-16	1.990 ± 0.016	S
57082.362	2015-02-28	1.910 ± 0.023	57082.362	2015-02-28	2.195 ± 0.020	S
57088.594	2015-03-07	2.028 ± 0.034	57088.594	2015-03-07	2.200 ± 0.025	S
57100.539	2015-03-19	1.883 ± 0.004	57100.539	2015-03-19	2.172 ± 0.016	S
57112.285	2015-03-30	1.741 ± 0.018	57112.285	2015-03-30	2.080 ± 0.020	S
57121.256	2015-04-08	1.788 ± 0.011	57121.256	2015-04-08	2.133 ± 0.015	S
57130.736	2015-04-18	1.990 ± 0.032	57130.755	2015-04-18	2.186 ± 0.024	V16
57131.243	2015-04-18	1.925 ± 0.011	57131.243	2015-04-18	2.198 ± 0.021	S
57132.313	2015-04-19	1.940 ± 0.081	57132.313	2015-04-19	2.300 ± 0.110	SW
57132.712	2015-04-20	1.947 ± 0.026	57132.731	2015-04-20	2.285 ± 0.017	V16
57133.659	2015-04-21	1.934 ± 0.048	57133.677	2015-04-21	2.294 ± 0.013	V16
57134.681	2015-04-22	1.938 ± 0.034	57134.700	2015-04-22	2.353 ± 0.021	V16
57138.750	2015-04-26	1.690 ± 0.070	57138.750	2015-04-26	2.120 ± 0.090	SW
57140.653	2015-04-28	1.786 ± 0.029	57140.672	2015-04-28	2.168 ± 0.019	V16
57141.604	2015-04-29	1.747 ± 0.040	57141.622	2015-04-29	2.128 ± 0.015	V16
57142.602	2015-04-30	1.770 ± 0.034	57142.620	2015-04-30	2.186 ± 0.020	V16
			57145.670	2015-05-03	2.163 ± 0.023	V16
57145.837	2015-05-03	1.750 ± 0.081	57145.837	2015-05-03	2.200 ± 0.110	SW
57147.651	2015-05-05	1.662 ± 0.034				V16
57148.656	2015-05-06	1.663 ± 0.023	57148.675	2015-05-06	2.056 ± 0.015	V16
			57150.644	2015-05-08	2.331 ± 0.022	V16
57151.581	2015-05-09	1.704 ± 0.029	57151.600	2015-05-09	2.179 ± 0.023	V16
57151.663	2015-05-09	1.686 ± 0.039				BII
57152.688	2015-05-10	1.650 ± 0.061	57152.688	2015-05-10	2.130 ± 0.080	SW
57152.727	2015-05-10	1.606 ± 0.027				BII
57153.585	2015-05-11	1.580 ± 0.018	57153.603	2015-05-11	2.027 ± 0.016	V16
57153.636	2015-05-11	1.582 ± 0.029				BII
57156.555	2015-05-14	1.587 ± 0.020	57156.574	2015-05-14	1.976 ± 0.014	V16
57156.667	2015-05-14	1.651 ± 0.026				BII
57157.663	2015-05-15	1.651 ± 0.030	57157.556	2015-05-15	1.979 ± 0.014	BII, V16

Continuum flux in units of  $10^{-15} \text{ erg s}^{-1} \text{ cm}^{-2} \text{ Å}^{-1}$ .

Table 4. continued.

Julian Date 2 400 000+	UT Date	Cont. Flux 4570 Å, B band	Julian Date 2 400 000+	UT Date	Cont. Flux 5360 Å, V band	Tel.
57158.735	2015-05-16	1.529 ± 0.037	57158.653	2015-05-16	2.035 ± 0.036	BII, V16
57160.681	2015-05-18	1.700 ± 0.018				BII
57160.903	2015-05-18	1.590 ± 0.090	57160.903	2015-05-18	2.120 ± 0.140	SW
57161.637	2015-05-19	1.637 ± 0.029	57161.555	2015-05-19	2.060 ± 0.034	V16
57162.639	2015-05-20	1.668 ± 0.025	57162.606	2015-05-20	2.125 ± 0.042	V16
57163.722	2015-05-21	1.760 ± 0.038	57163.553	2015-05-21	2.013 ± 0.041	V16
57164.639	2015-05-22	1.721 ± 0.024	57164.553	2015-05-22	2.034 ± 0.035	V16
			57165.658	2015-05-23	2.057 ± 0.036	V16
57167.083	2015-05-24	1.760 ± 0.070	57167.083	2015-05-24	2.090 ± 0.090	SW
57167.359	2015-05-24	1.724 ± 0.019	57167.359	2015-05-24	2.099 ± 0.019	S
			57169.598	2015-05-27	2.018 ± 0.031	V16
57170.546	2015-05-28	1.770 ± 0.047	57170.533	2015-05-28	2.108 ± 0.014	BII, V16
57171.364	2015-05-28	1.699 ± 0.012	57171.364	2015-05-28	2.056 ± 0.022	S
57171.601	2015-05-29	1.575 ± 0.028	57171.554	2015-05-29	2.028 ± 0.019	BII, V16
57173.816	2015-05-31	1.740 ± 0.081	57173.816	2015-05-31	2.050 ± 0.100	SW
57174.628	2015-06-01	1.568 ± 0.040	57174.586	2015-06-01	1.965 ± 0.021	BII, V16
57175.595	2015-06-02	1.548 ± 0.032	57175.553	2015-06-02	2.047 ± 0.019	BII, V16
57176.595	2015-06-03	1.596 ± 0.041	57176.558	2015-06-03	2.089 ± 0.024	BII, V16
			57177.614	2015-06-04	1.967 ± 0.014	V16
57178.595	2015-06-05	1.716 ± 0.034	57178.566	2015-06-05	2.020 ± 0.019	BII, V16
57179.595	2015-06-06	1.525 ± 0.029	57179.552	2015-06-06	2.016 ± 0.020	BII, V16
57180.596	2015-06-07	1.530 ± 0.030	57180.568	2015-06-07	2.029 ± 0.021	BII, V16
57181.000	2015-06-07	1.530 ± 0.061	57181.000	2015-06-07	1.970 ± 0.080	SW
57181.596	2015-06-08	1.502 ± 0.032	57181.552	2015-06-08	1.998 ± 0.014	BII, V16
57182.330	2015-06-08	1.497 ± 0.010	57182.330	2015-06-08	1.950 ± 0.015	S
57182.600	2015-06-09	1.457 ± 0.022	57182.553	2015-06-09	2.036 ± 0.012	BII, V16
57183.570	2015-06-10	1.527 ± 0.027	57183.515	2015-06-10	1.978 ± 0.014	BII, V16
57184.569	2015-06-11	1.506 ± 0.018	57184.515	2015-06-11	1.954 ± 0.014	BII, V16
57185.569	2015-06-12	1.576 ± 0.035	57185.515	2015-06-12	2.053 ± 0.012	BII, V16
57186.570	2015-06-13	1.511 ± 0.032	57186.515	2015-06-13	1.983 ± 0.010	BII, V16
57187.319	2015-06-13	1.445 ± 0.018	57187.319	2015-06-13	1.941 ± 0.011	S
57187.570	2015-06-14	1.467 ± 0.026	57187.516	2015-06-14	1.990 ± 0.012	BII, V16
57187.806	2015-06-14	1.430 ± 0.061	57187.806	2015-06-14	2.010 ± 0.090	SW
			57189.516	2015-06-16	1.998 ± 0.019	V16
57192.308	2015-06-18	1.600 ± 0.011	57192.308	2015-06-18	2.023 ± 0.019	S
			57192.518	2015-06-19	2.012 ± 0.020	V16
57195.424	2015-06-21	1.470 ± 0.070	57195.424	2015-06-21	1.980 ± 0.090	SW
57195.510	2015-06-22	1.476 ± 0.022	57195.497	2015-06-21	1.948 ± 0.014	BII, V16
57196.295	2015-06-22	1.608 ± 0.013	57196.295	2015-06-22	2.020 ± 0.017	S
			57198.497	2015-06-24	1.970 ± 0.017	V16
57201.271	2015-06-27	1.467 ± 0.010	57201.271	2015-06-27	1.944 ± 0.017	S
57201.879	2015-06-28	1.490 ± 0.070	57201.879	2015-06-28	1.950 ± 0.100	SW
57203.486	2015-06-29	1.617 ± 0.032	57203.461	2015-06-29	2.005 ± 0.013	BII, V16
57206.265	2015-07-02	1.705 ± 0.014	57206.265	2015-07-02	2.098 ± 0.018	S
57209.188	2015-07-05	1.660 ± 0.061	57209.188	2015-07-05	2.060 ± 0.090	SW
57211.488	2015-07-07	1.613 ± 0.023				BII
57212.488	2015-07-08	1.654 ± 0.030				BII
57213.491	2015-07-09	1.625 ± 0.038				BII
57215.489	2015-07-11	1.619 ± 0.029				BII
57216.519	2015-07-13	1.624 ± 0.038				BII
57217.227	2015-07-13	1.718 ± 0.030	57217.227	2015-07-13	2.117 ± 0.025	S
57218.219	2015-07-14	1.590 ± 0.070	57218.219	2015-07-14	1.880 ± 0.090	SW
57222.629	2015-07-19	1.510 ± 0.061	57222.629	2015-07-19	1.980 ± 0.090	SW
57229.917	2015-07-26	1.560 ± 0.070	57229.917	2015-07-26	2.030 ± 0.090	SW
57236.969	2015-08-02	1.580 ± 0.070	57236.969	2015-08-02	2.090 ± 0.090	SW
57337.576	2015-11-11	1.950 ± 0.081	57337.576	2015-11-11	2.130 ± 0.100	SW
57399.510	2016-01-12	1.913 ± 0.017	57399.510	2016-01-12	2.240 ± 0.020	S
57421.351	2016-02-02	2.000 ± 0.070	57421.351	2016-02-02	2.340 ± 0.100	SW
			57473.593	2016-03-26	2.084 ± 0.014	V16

Continuum flux in units of  $10^{-15} \text{ erg s}^{-1} \text{ cm}^{-2} \text{ Å}^{-1}$ .

Table 4. continued.

Julian Date 2 400 000+	UT Date	Cont. Flux 4570 Å, B band	Julian Date 2 400 000+	UT Date	Cont. Flux 5360 Å, V band	Tel.
57474.588	2016-03-27	1.748 ± 0.025	57474.570	2016-03-27	1.956 ± 0.013	V16
57475.558	2016-03-28	1.647 ± 0.017	57475.540	2016-03-28	1.977 ± 0.010	V16
57477.599	2016-03-30	1.616 ± 0.018	57477.581	2016-03-30	1.856 ± 0.013	V16
57478.581	2016-03-31	1.659 ± 0.017	57478.563	2016-03-31	1.968 ± 0.013	V16
57479.555	2016-04-01	1.687 ± 0.018	57479.537	2016-04-01	1.874 ± 0.011	V16
57480.747	2016-04-02	1.636 ± 0.018	57480.729	2016-04-02	1.974 ± 0.015	V16
57481.686	2016-04-03	1.697 ± 0.019	57481.668	2016-04-03	1.888 ± 0.012	V16
57482.737	2016-04-04	1.691 ± 0.018	57482.676	2016-04-04	1.980 ± 0.014	V16
57484.606	2016-04-06	1.702 ± 0.017	57484.587	2016-04-06	1.913 ± 0.010	V16
57485.552	2016-04-07	1.724 ± 0.016	57485.534	2016-04-07	1.932 ± 0.008	V16
57486.667	2016-04-08	1.775 ± 0.015	57486.649	2016-04-08	1.967 ± 0.013	V16
57487.577	2016-04-09	1.772 ± 0.020	57487.558	2016-04-09	1.975 ± 0.014	V16
57488.553	2016-04-10	1.820 ± 0.024	57488.535	2016-04-10	2.037 ± 0.011	V16
57492.493	2016-04-13	1.945 ± 0.025	57492.475	2016-04-13	2.177 ± 0.021	V16
57493.515	2016-04-15	1.941 ± 0.026	57493.497	2016-04-14	2.061 ± 0.014	V16
57494.495	2016-04-15	1.991 ± 0.025	57494.477	2016-04-15	2.112 ± 0.014	V16
57499.489	2016-04-20	1.893 ± 0.038	57499.471	2016-04-20	2.148 ± 0.017	V16
57500.488	2016-04-21	1.897 ± 0.034	57500.470	2016-04-21	2.181 ± 0.021	V16
57504.252	2016-04-25	1.854 ± 0.025	57504.253	2016-04-25	2.155 ± 0.012	MS
57505.513	2016-04-27	1.839 ± 0.077	57505.514	2016-04-27	2.140 ± 0.024	MS
57507.599	2016-04-29	1.840 ± 0.018	57507.581	2016-04-29	2.123 ± 0.015	V16
57508.497	2016-04-29	1.797 ± 0.017	57508.478	2016-04-29	2.011 ± 0.015	V16
57509.484	2016-04-30	1.865 ± 0.021	57509.466	2016-04-30	2.031 ± 0.020	V16
57510.565	2016-05-02	1.879 ± 0.024	57510.547	2016-05-02	2.070 ± 0.019	V16
57511.399	2016-05-02	1.826 ± 0.023				MS
57511.530	2016-05-03	1.920 ± 0.017	57511.512	2016-05-03	2.114 ± 0.010	V16
57512.489	2016-05-03	1.895 ± 0.018	57512.470	2016-05-03	2.082 ± 0.014	V16
57513.282	2016-05-04	2.018 ± 0.016	57513.284	2016-05-04	2.323 ± 0.021	MS
57514.333	2016-05-05	2.017 ± 0.015	57514.334	2016-05-05	2.365 ± 0.020	MS
57515.553	2016-05-07	2.032 ± 0.023	57515.533	2016-05-07	2.369 ± 0.014	V16
57516.517	2016-05-08	2.132 ± 0.018	57516.499	2016-05-07	2.329 ± 0.021	V16
57518.273	2016-05-09	1.873 ± 0.025	57518.274	2016-05-09	2.174 ± 0.011	MS
57519.391	2016-05-10	1.944 ± 0.005	57519.391	2016-05-10	2.311 ± 0.014	S
57520.353	2016-05-11	1.862 ± 0.026	57520.354	2016-05-11	2.171 ± 0.012	MS
57521.629	2016-05-13	1.955 ± 0.025	57521.647	2016-05-13	2.299 ± 0.016	V16
57522.461	2016-05-13	1.866 ± 0.018	57522.479	2016-05-13	2.100 ± 0.014	V16
57524.471	2016-05-15	1.752 ± 0.025	57524.490	2016-05-15	2.014 ± 0.033	V16
57526.462	2016-05-17	1.731 ± 0.023				V16
57527.460	2016-05-18	1.558 ± 0.025				V16
57529.463	2016-05-20	1.789 ± 0.039				V16
57530.295	2016-05-21	1.740 ± 0.256	57530.296	2016-05-21	2.137 ± 0.114	MS
57530.459	2016-05-21	1.728 ± 0.022				V16
57531.639	2016-05-23	1.652 ± 0.044				V16
57532.509	2016-05-24	1.636 ± 0.018				V16
57533.458	2016-05-24	1.705 ± 0.022				V16
57534.519	2016-05-26	1.839 ± 0.024				V16
57535.293	2016-05-26	1.784 ± 0.023	57535.294	2016-05-26	2.130 ± 0.011	MS
57536.314	2016-05-27	1.804 ± 0.023	57536.315	2016-05-27	2.133 ± 0.011	MS
57536.458	2016-05-27	1.805 ± 0.025				V16
57537.309	2016-05-28	1.915 ± 0.013	57537.310	2016-05-28	2.240 ± 0.013	MS
57538.230	2016-05-29	1.927 ± 0.014	57538.232	2016-05-29	2.262 ± 0.013	MS
57538.626	2016-05-30	1.900 ± 0.046				V16
57539.487	2016-05-30	1.908 ± 0.018				V16
57540.351	2016-05-31	1.888 ± 0.008	57540.351	2016-05-31	2.196 ± 0.018	S
57540.599	2016-06-01	1.902 ± 0.063				V16
57541.542	2016-06-02	1.843 ± 0.032				V16
57542.536	2016-06-03	1.960 ± 0.028				V16
57546.234	2016-06-06	1.822 ± 0.023	57546.236	2016-06-06	2.173 ± 0.011	MS
57551.512	2016-06-12	2.086 ± 0.035				V16

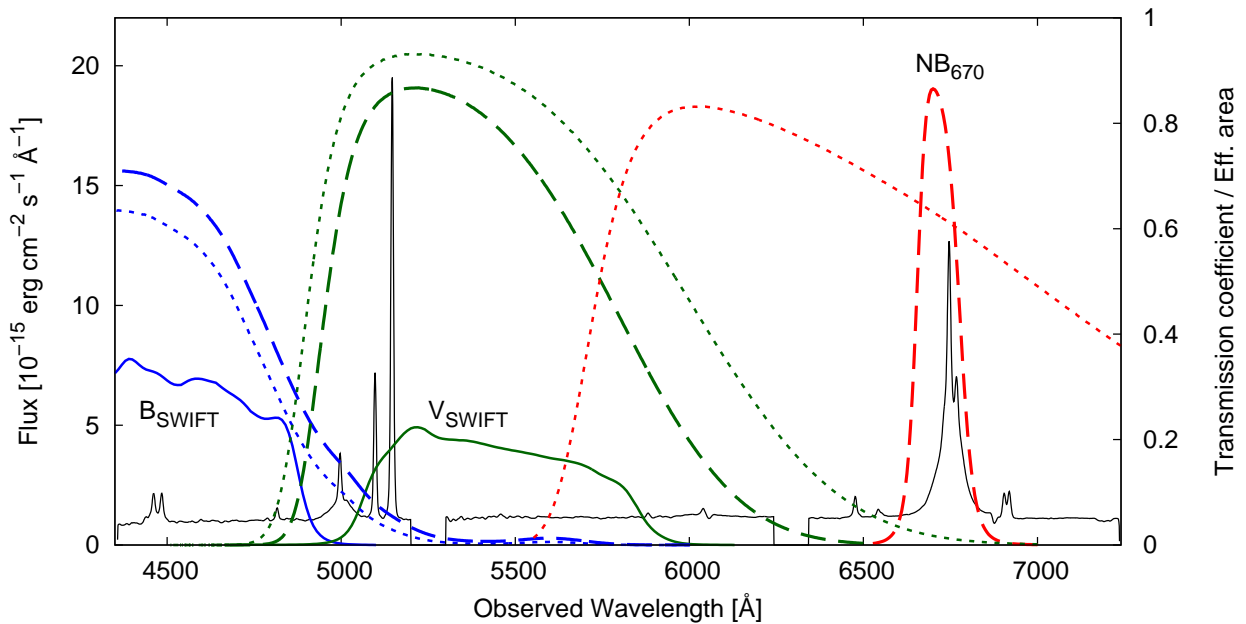
Continuum flux in units of  $10^{-15} \text{ erg s}^{-1} \text{ cm}^{-2} \text{ Å}^{-1}$ .



Table 4. continued.

Julian Date 2 400 000+	UT Date	Cont. Flux 4570 Å, B band	Julian Date 2 400 000+	UT Date	Cont. Flux 5360 Å, V band	Tel.
57555.463	2016-06-15	2.030 ± 0.024				V16
57558.358	2016-06-18	1.692 ± 0.250	57558.359	2016-06-18	2.145 ± 0.098	MS
57558.459	2016-06-18	1.860 ± 0.022				V16
57560.459	2016-06-20	1.994 ± 0.038				V16
57561.329	2016-06-21	1.897 ± 0.103	57561.330	2016-06-21	2.215 ± 0.031	MS
57561.463	2016-06-21	1.969 ± 0.018				V16
57562.459	2016-06-22	2.152 ± 0.028				V16
57567.460	2016-06-27	2.000 ± 0.027	57567.480	2016-06-27	2.277 ± 0.022	V16
57569.461	2016-06-29	1.881 ± 0.023	57569.480	2016-06-29	2.165 ± 0.021	V16
57575.467	2016-07-05	2.105 ± 0.031	57575.486	2016-07-05	2.451 ± 0.016	V16
57581.468	2016-07-11	2.080 ± 0.023				V16
57582.469	2016-07-12	2.159 ± 0.028				V16
57583.468	2016-07-13	2.214 ± 0.025				V16
57584.464	2016-07-14	2.141 ± 0.031				V16
57585.504	2016-07-16	2.059 ± 0.032				V16
57889.381	2017-05-15	1.997 ± 0.017	57889.381	2017-05-15	2.263 ± 0.016	S

Continuum flux in units of  $10^{-15} \text{ erg s}^{-1} \text{ cm}^{-2} \text{ \AA}^{-1}$ .



**Fig. 1.** Mean spectrum of HE 1136-2304 based on the observations performed with the SALT telescope together with the effective areas of the *Swift* B and V bandpass curves (in units of  $\text{cm}^2$  divided by 100) (solid lines); the Bochum B, V, and  $\text{NB}_{670}$  filter curves (dashed lines); and the MONET B, V, and R filter curves (dotted lines).

Table 4 gives the derived B and V fluxes of HE 1136-2304 based on the *Swift* data, SALT spectra, photometric data obtained with the Cerro Armazones, and the MONET/North and South telescopes from 2014 to 2017. All these photometric data have been intercalibrated with respect to the *Swift* data. In addition, we list the B and V values based on the ESO spectrum taken in 1993 (Reimers et al. 1996), and those based on the 6dF spectrum taken in 2002 (Jones et al. 2004).

Figure 5 shows the X-ray, UV, and optical *Swift* light curves for our detailed campaign in 2015 from April until August in one plot to compare their amplitudes. During these months the source was observed weekly. Figure 5 is a zoom-in of the middle part of Figure 4. The UV and optical *Swift* bands closely follow the X-ray light curve. The X-ray light curve exhibits the strongest variability amplitudes. On the other hand, the *Swift* V band only shows minor variations in contrast to the other bands.

Table 5 gives the variability statistics based on the *Swift* continua (XRT, W2, M2, W1, U, B, V). We indicate the minimum and maximum fluxes  $F_{\min}$  and  $F_{\max}$ , peak-to-peak amplitudes  $R_{\max} = F_{\max}/F_{\min}$ , the mean flux over the period of observations  $\langle F \rangle$ , the standard deviation  $\sigma_F$ , and the fractional variation

$$F_{\text{var}} = \frac{\sqrt{\sigma_F^2 - \Delta^2}}{\langle F \rangle},$$

as defined by Rodríguez-Pascual et al. (1997). The quantity  $\Delta^2$  is the mean square value of the uncertainties  $\Delta_i$  associated with the fluxes  $F_i$ . The  $F_{\text{var}}$  uncertainties are defined in Edelson et al. (2002). The peak-to-peak amplitude and the fractional variation decrease as a function of wavelength. Additionally, we present the variability statistics based on the combined B and V light curves including all optical ground-based telescopes (MONET, Cerro Armazones, SALT) and *Swift* in units of  $10^{-15} \text{ erg s}^{-1} \text{ cm}^{-2} \text{ \AA}^{-1}$ . The results are similar to those based on the *Swift* data only. Furthermore, we give the variability statistics based solely on the dedicated variability campaign in 2015. In comparison to the complete data set, the peak-to-peak amplitudes and the fractional variations are smaller because the optical high state in 2014 is not included (see Figures 2 and 3).

We compare our results with those from other spectroscopic AGN variability campaigns. In comparison to photometric campaigns, these spectroscopic variability campaigns are typically based on small apertures. Therefore, we additionally calculated the variability statistics based on our small aperture spectral data taken with SALT without intercalibration with respect to the large aperture photometric data.

Finally, we present the variability statistics after subtracting the nonvariable flux contribution of the host galaxy. This results in significantly higher variability amplitudes in all individual wavebands (Table 5, Col. 2). The derivation of the host galaxy flux contribution is described in the following two sections.

### 3.2. Host galaxy contribution to the optical continuum flux

Figure 6 displays the DSS1 image of HE 1136-2304 (Scale:  $2 \times 2$  arcmin; pixel size 1.7 arcsec) as well as a B-V two-color image (bottom) based on VYSOS 16 data. The nucleus of HE 1136-2304 is surrounded by a spiral or S0 host galaxy; the radial profile of the surface brightness shows a central bulge structure and an extended disk structure in the DSS1 image. Some asymmetry of the outer isophotes might be connected with the object located to the east at a distance of 12 arcsec.

The observed flux of the variable AGN component is contaminated by the flux contribution of the host galaxy. The rela-

tive contribution of the host galaxy in the individual bands differs since the central nonthermal component has a different flux distribution from the stellar component of the host galaxy. Furthermore, the flux contribution of the host galaxy depends on the size of the aperture. In addition, we compare the accuracy and the results based on the photometric observations taken with *Swift* on the one hand and spectroscopic observations taken with SALT on the other hand. These photometric and spectroscopic observations were carried out with different apertures. All other photometric data were intercalibrated with respect to the absolute fluxes of *Swift*. Finally, we compare our results with those of Parker et al. (2016). Their results are based on only two spectra obtained in 1993 and 2014 and taken with different instruments and apertures.

We estimate the relative contribution of the constant host galaxy flux by means of the flux variation gradient (FVG) method (Choloniewski 1981, Winkler et al. 1992, Haas et al. 2011, Ramolla et al. 2015). This method disentangles the varying AGN flux in our aperture from the constant host galaxy contribution. We obtained B and V flux values of HE 1136-2304 based on the 5" aperture of the *Swift* UVOT. Furthermore, we derived B-, V-, and R-band fluxes for the SALT spectra by convolving them with the B, V, and R filter curves (IRAF task *sbands*). We measured the fluxes at wavelengths close to the maxima of the filter curves (B-band filter: 4300 Å; V-band filter: 5400 Å; R-band filter: 6100 Å) with widths of a few hundred Å. In this way we excluded the contribution of emission lines in the spectra (see Fig. 1). These B, V, and R values are presented in Table 6.

Figures 7 and 8 show the B versus V and B versus R fluxes (black solid circles) of HE 1136-2304 based on the SALT spectra (aperture:  $2 \times 2$  arcsec). The blue dashed line gives the best linear fit to the B versus V and B versus R fluxes. The black solid lines cover the upper and lower standard deviations of the interpolated AGN slope. The red dashed lines give the range of host slopes for nearby AGN as determined by Sakata et al. (2010). The intersection point between the AGN and host galaxy slopes gives the host galaxy fluxes in the B, V, and R bands. The gray lines indicate these B, V, and R values of the host galaxy.

Based on the intersection in the two figures, we derive a B-band flux of 0.27 mJy for the host galaxy contribution (mean of 0.25 and 0.29 mJy). The corresponding values are 0.57 mJy for the V band and 0.85 mJy for the R band. Our derived flux values for the contribution of the host galaxy in the B- and R-band spectra are 15% higher than those derived in Parker et al. (2016). The new values are of higher confidence. They are based on spectra taken under identical conditions at 21 epochs. Parker et al. (2016) used only two spectra taken with different apertures. Figure 9 shows the B versus V flux variations based on the *Swift* photometric data taken with a 12 arcsec aperture.

Once we know the integrated flux values of the host galaxy plus AGN as well as the host galaxy contribution, we can derive the AGN flux contribution in the individual bands. All these values are listed in Table 7. We present these values separately for the measurements based on the SALT spectra (based on the smaller aperture) and for the *Swift* data (based on the larger aperture). Furthermore, we give all these flux values in units of mJy and in units of  $10^{-15} \text{ erg s}^{-1} \text{ cm}^{-2} \text{ \AA}^{-1}$  with the conversion formula

$$F_{\text{mJy},\lambda} = F \frac{\lambda^2}{29979245.8}, \quad (1)$$

where  $F_{\text{mJy},\lambda}$  is the flux in units of mJy,  $F$  the flux in units of  $10^{-15} \text{ erg s}^{-1} \text{ cm}^{-2} \text{ \AA}^{-1}$ , and  $\lambda$  the wavelength in Å.

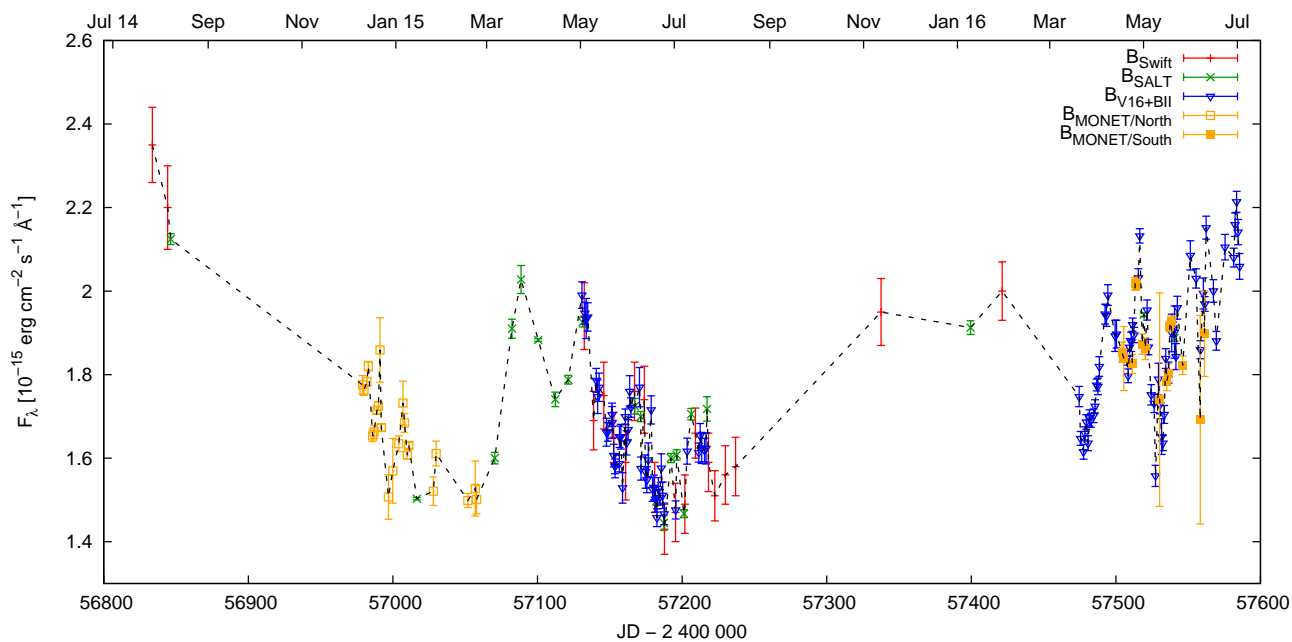


**Fig. 2.** Combined B-band continuum light curve (*Swift*, SALT, MONET, VYSOS-16, BEST II) calibrated with respect to the *Swift* data from 2014 to 2016. The time stamps at the top indicate the first day of the month.

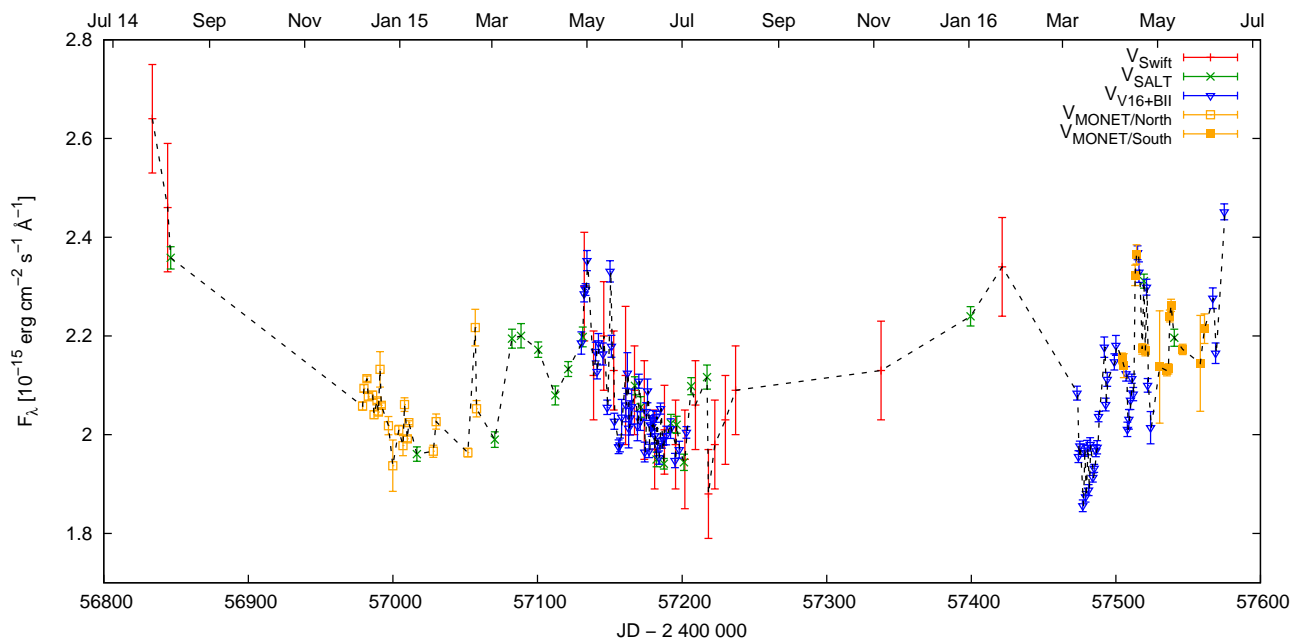


**Fig. 3.** Combined V-band continuum light curve (*Swift*, SALT, MONET, VYSOS-16, BEST II) calibrated with respect to the *Swift* data from 2014 to 2016. The time stamps at the top indicate the first day of the month.

The derived host galaxy fluxes in the B and V bands (based on the *Swift* data) are a factor two higher than those based on the SALT spectra because the larger extraction area of the *Swift* UVOT (10 arcsec diameter) collects more flux of the extended host galaxy than the SALT spectra do (2 x 2 arcsec only). However, the mean AGN fluxes derived on the basis of the SALT spectra are similar to those based on the *Swift* UVOT data (last three rows in Table 7). The AGN contribution based on the SALT spectra corresponds to 60%, 51%, and 41% in the B, V, and R band, respectively. The AGN contribution in the *Swift* UVOT B and V band decreases to 38% and 25%, respectively, because of their larger aperture.

### 3.3. *Swift* inter-band correlation analysis and host galaxy contribution in the UV/optical bands

The *Swift* X-ray, UV, and optical light curves based on the variability campaign in 2015 are shown in Figure 5. They all exhibit a similar variability pattern except for the V band, which exhibits no major variability amplitudes.

Based on these light curves we present the cross-correlation functions ICCF( $\tau$ ) of all the *Swift* UVOT bands with respect to the XRT light curve in Figure 10. In addition, we show the auto-correlation function (ACF) of the XRT band. We used the cross-correlation method as described in, e.g., Dietrich & Kollatschny (1995) and Kollatschny et al. (2014). Table 8 lists the maximum correlation coefficient  $r_{\max}$  of the individual *Swift* bands with re-

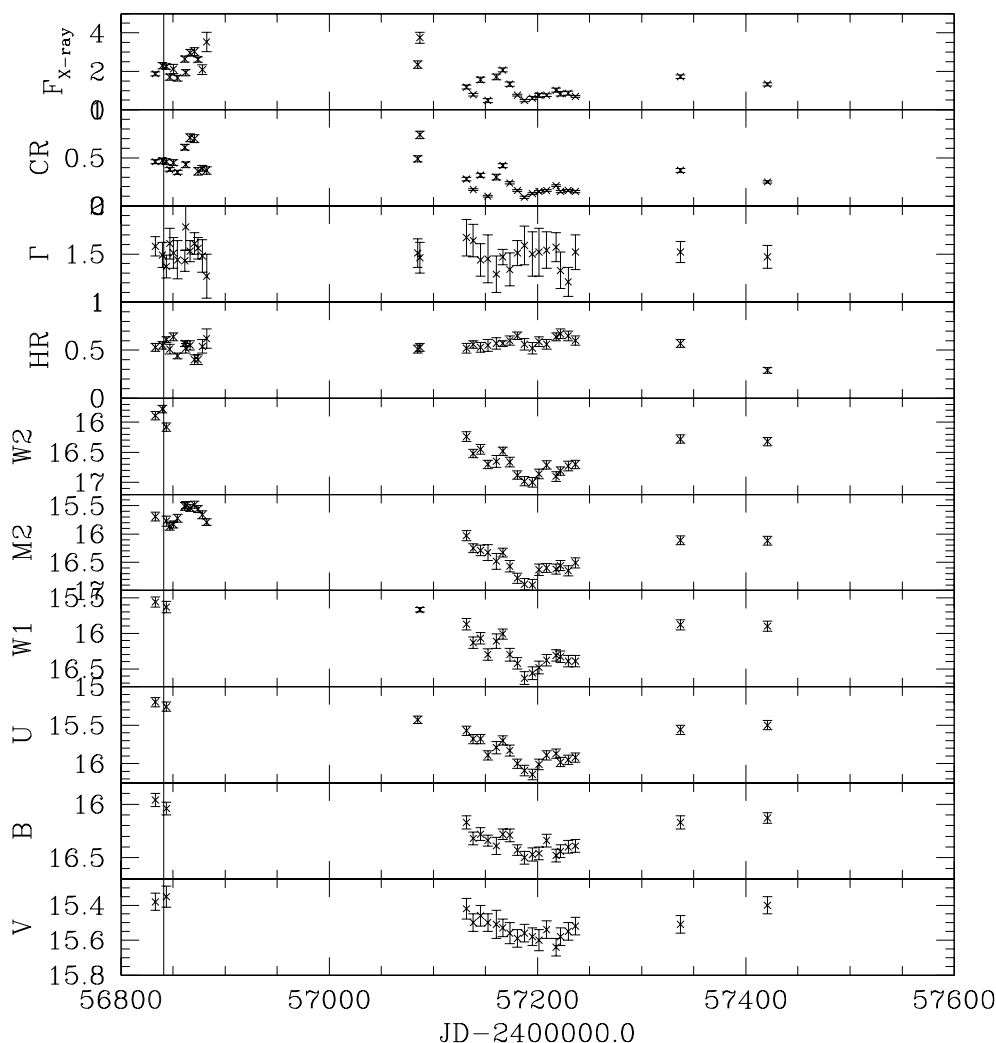


**Fig. 4.** *Swift* X-ray light curve from 2014 to 2016. The solid line at JD 2456841 marks the time of the XMM observation discussed in Parker et al. (2016). The observed 0.3–10 keV X-ray flux is given in units of  $10^{-11}$  ergs  $s^{-1}$   $cm^{-2}$ . The X-ray count rates (CR), the X-ray photon index  $\Gamma$  of a simple power-law model, and the hardness ratios (HR) are also shown. The UVOT W2, M2, W1, U, B, and V magnitudes are given in the Vega system.

spect to the XRT band as well as the lags with respect to the XRT band. We derive the centroids of these ICCF,  $\tau_{\text{cent}}$ , by using only the part of the CCF above 80% of the peak value. It has been shown by Peterson et al. (2003) that a threshold value of  $0.8 r_{\text{max}}$  is generally a good choice. We determine the uncertainties of our cross-correlation results by calculating the cross-correlation lags many times using a model-independent Monte Carlo method known as flux redistribution/random subset selection (FR/RSS). This method was described by Peterson et al. (1998). The uncertainties correspond to 68% confidence levels.

The V-band light curve does not show any significant correlation with respect to the X-ray light curve (see Figure 10). This might be caused by the nonthermal AGN contribution in the V band being less than 25% (see Table 7). Furthermore, the light distribution of the host galaxy is not exactly point-like, as seen in Figure 6. Therefore, measurements made with a large aperture in the V band are more sensitive to small-scale deviations from an exact centering. By contrast, the X-ray and UV bands are dominated by the central nonthermal point source. Additionally, the V band is contaminated by the variable H $\beta$  line (see Figure 1).

Figure 11 shows the time delay of the *Swift* UV and optical bands with respect to the *Swift* X-ray light curve as a function

of wavelength. The V band has been excluded here as it showed no correlation. The dashed line shows the most general fit to the data:

$$\tau = b((\lambda/\lambda_0)^c - 1)$$

with  $\lambda_0 = 25 \text{ \AA}$ . The b-value and the power-law index c have been allowed to vary. First we determined the fit parameter  $b = 0.003 \pm 0.020$  light-days giving a hint on the size of the X-ray emitting region at  $\lambda_0 = 25 \text{ \AA}$  (corresponding to  $\lambda_{\text{pivot}}$  of XRT filter). Afterwards we kept b fixed and calculated the exponent c. The best fit to the data gives  $c = 1.3 \pm 0.1$ . This value is consistent with a theoretically expected value  $c = 1.33 = 4/3$  for an irradiated accretion disk (see discussion section).

The UV and optical spectral energy distribution of HE 1136-2304 based on our *Swift* data taken in 2015 is presented in Figure 12 with black symbols. The red open circles show the contribution of the host galaxy in the individual bands. The host contribution in the B and V bands is based on the flux variation gradient analysis (section 3.2). We calculated the contribution of the host galaxy in the UV bands by scaling an Sb spectrum (Kinney et al. 1996) with respect to the B and V fluxes of the host galaxy.

**Table 5.** Variability statistics based on the *Swift* continua (XRT, W2, M2, W1, U, B, V) and on the combined B and V light curves (*Swift*, SALT, MONET, Cerro Armazones) in units of  $10^{-15}$  erg s $^{-1}$  cm $^{-2}$  Å $^{-1}$  and  $10^{-11}$  ergs s $^{-1}$  cm $^{-2}$  for the 0.3–10 keV X-ray data. In addition, we give the statistics solely for the dedicated campaign in 2015. Finally, we present the variability statistics based solely on the SALT spectra with their small aperture. In the second column the variability statistics is given after subtraction of the host galaxy flux.

Cont.	with host						without host					
	F <sub>max</sub>	F <sub>min</sub>	R <sub>max</sub>	<F>	σ <sub>F</sub>	F <sub>var</sub>	F <sub>max</sub>	F <sub>min</sub>	R <sub>max</sub>	<F>	σ <sub>F</sub>	F <sub>var</sub>
(1)	(2)	(3)	(4)	(5)	(6)	(7)	(8)	(9)	(10)	(11)	(12)	(13)
Cont. <i>Swift</i> XRT all	3.75	0.48	7.81	1.65	0.86	0.516 ± 0.016						
Cont. <i>Swift</i> W2 all	1.83	0.66	2.77	1.00	0.31	0.308 ± 0.015	1.58	0.41	3.88	0.74	0.31	0.413 ± 0.020
Cont. <i>Swift</i> M2 all	2.22	0.60	3.71	1.31	0.53	0.402 ± 0.009	1.99	0.37	5.43	1.08	0.53	0.488 ± 0.011
Cont. <i>Swift</i> W1 all	1.92	0.71	2.69	1.14	0.34	0.288 ± 0.016	1.64	0.44	3.74	0.86	0.34	0.380 ± 0.021
Cont. <i>Swift</i> U all	2.49	1.05	2.37	1.53	0.40	0.253 ± 0.012	1.99	0.55	3.60	1.03	0.40	0.375 ± 0.018
Cont. <i>Swift</i> B all	2.35	1.43	1.64	1.72	0.25	0.138 ± 0.010	1.40	0.48	2.93	0.77	0.25	0.309 ± 0.022
Cont. <i>Swift</i> V all	2.64	1.88	1.40	2.13	0.19	0.073 ± 0.012	1.27	0.51	2.49	0.76	0.19	0.206 ± 0.033
Cont. B all	2.35	1.43	1.64	1.76	0.19	0.103 ± 0.002	1.40	0.48	2.93	0.80	0.19	0.224 ± 0.004
Cont. V all	2.64	1.86	1.42	2.09	0.13	0.058 ± 0.002	1.27	0.49	2.62	0.72	0.13	0.167 ± 0.005
Cont. <i>Swift</i> XRT 2015	2.07	0.48	4.31	0.99	0.46	0.452 ± 0.025						
Cont. <i>Swift</i> W2 2015	1.34	0.66	2.03	0.88	0.18	0.198 ± 0.017	1.09	0.41	2.67	0.62	0.18	0.278 ± 0.024
Cont. <i>Swift</i> M2 2015	1.34	0.60	2.24	0.87	0.20	0.217 ± 0.019	1.11	0.37	3.03	0.64	0.20	0.296 ± 0.025
Cont. <i>Swift</i> W1 2015	1.44	0.71	2.01	1.00	0.19	0.178 ± 0.021	1.16	0.44	2.65	0.72	0.19	0.246 ± 0.029
Cont. <i>Swift</i> U 2015	1.77	1.05	1.69	1.35	0.20	0.138 ± 0.015	1.27	0.55	2.30	0.86	0.20	0.218 ± 0.023
Cont. <i>Swift</i> B 2015	1.94	1.43	1.36	1.62	0.13	0.069 ± 0.012	0.99	0.48	2.07	0.67	0.13	0.168 ± 0.029
Cont. <i>Swift</i> V 2015	2.30	1.88	1.22	2.06	0.10	0.017 ± 0.026	0.93	0.51	1.82	0.69	0.10	0.051 ± 0.078
Cont. B 2015, Feb.–Aug.	2.03	1.43	1.42	1.66	0.14	0.081 ± 0.003	1.07	0.48	2.25	0.70	0.14	0.192 ± 0.007
Cont. V 2015, Feb.–Aug.	2.35	1.88	1.25	2.07	0.10	0.043 ± 0.003	0.98	0.51	1.93	0.70	0.10	0.128 ± 0.009
Cont. 4570 SALT 2015	1.26	0.78	1.61	0.99	0.14	0.141 ± 0.003	0.72	0.25	2.90	0.45	0.14	0.307 ± 0.007
Cont. 5360 SALT 2015	1.20	0.86	1.39	1.03	0.12	0.114 ± 0.006	0.64	0.31	2.08	0.47	0.12	0.248 ± 0.012

**Table 6.** Julian date, UT date, and B, V, and R values (in units of mJy) determined by convolving the SALT spectra with the corresponding filter curves.

Julian Date 2 400 000+	UT Date	B band	V band [mJy]	R band
56846.248	2014-07-07	0.87	1.42	1.74
57016.559	2014-12-25	0.52	1.03	1.28
57070.399	2015-02-16	0.63	1.03	1.27
57082.362	2015-02-28	0.75	1.28	1.53
57088.594	2015-03-07	0.81	1.36	1.67
57100.539	2015-03-19	0.79	1.20	1.47
57112.285	2015-03-30	0.66	1.08	1.37
57121.256	2015-04-08	0.69	1.11	1.39
57131.243	2015-04-18	0.77	1.18	1.49
57167.359	2015-05-24	0.64	1.22	1.43
57171.364	2015-05-28	0.62	1.10	1.40
57182.330	2015-06-08	0.53	0.93	1.18
57187.319	2015-06-13	0.49	0.91	1.16
57192.308	2015-06-18	0.56	1.24	1.57
57196.295	2015-06-22	0.55	1.05	1.36
57201.271	2015-06-27	0.48	0.88	1.13
57206.265	2015-07-02	0.63	1.13	1.43
57217.227	2015-07-13	0.62	1.11	1.42
57399.510	2016-01-12	0.81	1.25	1.57
57519.391	2016-05-10	0.89	1.38	1.64
57540.351	2016-05-31	0.81	1.29	1.61

The AGN flux in the individual bands has been determined by subtracting the flux of the host galaxy from the observed flux.

The blue filled squares in Figure 12 give the AGN flux contribution in the individual *Swift* bands. Knowing the AGN flux contribution in the individual *Swift* bands, we can derive the pure fractional variations in those bands. We present the fractional variations of the UV and optical continuum bands recorded with *Swift* in 2015 as a function of wavelength in Figure 13. The contribution of the host galaxy flux has been subtracted from the individual filter bands. We then add (in red) the fractional variations in the B and V bands on basis of our measurements with the different telescopes in 2015. There is a clear trend of increasing fractional variation of the AGN towards the UV. The dashed line shows a general fit to the data with a value  $c = 0.84$ .

We present the fractional variation of the X-ray band together with the fractional variations of the UV/optical bands in Figure 14. The fractional variations in X-rays are the strongest (as seen in Table 5). However, the fractional variations in X-rays do not follow the same trend as seen for the fractional variations in the UV and optical bands. An extrapolation of the fit in the UV and optical bands does not line up with the X-ray observations. This is an indication that the origin of the X-ray continuum emission is not connected in a simple way with the origin of the UV/optical emission (see Section 4.2).

#### 3.4. Spectral type changes and long-term variability of HE 1136-2304

The first spectrum of HE 1136-2304 was taken in 1993 (Reimers et al. 1996). At that time no broad H $\beta$  emission line component was present in the spectrum. Only a faint broad H $\alpha$  component was visible. Therefore, this galaxy was of nearly Seyfert 2 (1.95)

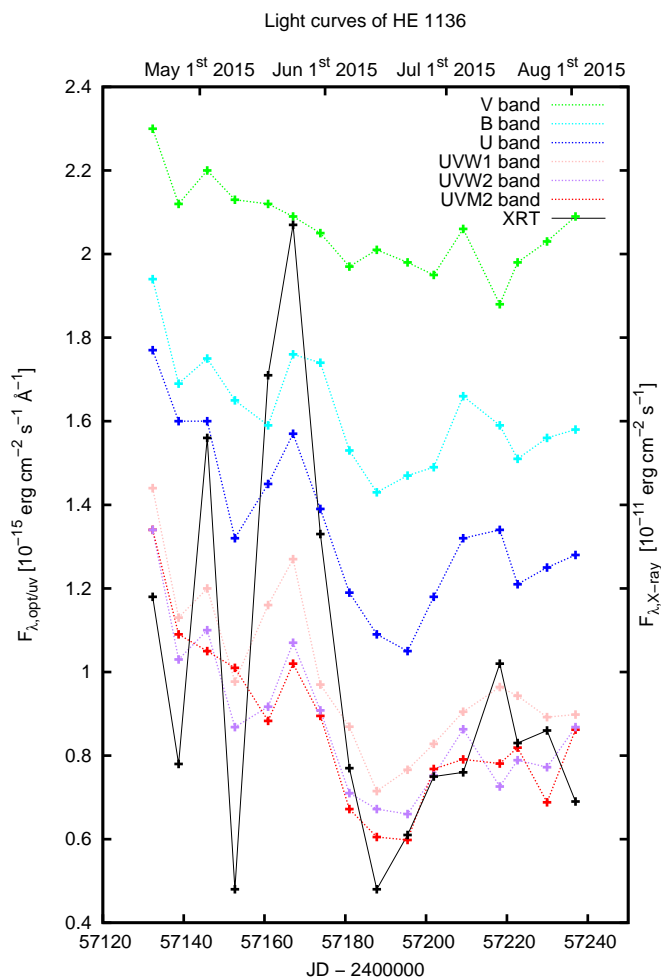


**Fig. 5.** Combined optical, UV, and X-ray light curves taken with the *Swift* satellite for the dedicated campaign in 2015.

type in 1993. Another spectrum of HE 1136-2304 was obtained on 2002 May 16 as part of the 6dF Galaxy Survey (Jones et al. 2004). At this time HE 1136-2304 was of the same spectral AGN type as it was nine years earlier. The AGN type had changed to Seyfert 1.5 when we took an optical spectrum in 2014 July (Parker et al. 2016). This happened together with an increase in the optical continuum flux and with a strong increase in X-ray flux.

In Figure 15 the spectra of HE 1136-2304 taken in 1993, 2002, 2014, 2015, 2016, and 2017 are shown to present line profile changes. The spectra are shifted by a constant with respect to each other. Figures 16 and 17 show the  $H\beta$  and  $H\alpha$  spectral regions in more detail. The mean spectrum for 2015 is based on the variability campaign carried out in 2015. We will present details of this campaign in a separate publication. The spectrum shown for 2016 is the mean of two spectra taken in May 2016. The strong broad component in the  $H\beta$  line profile that appeared in 2014 remained there for the subsequent years until 2017. No major profile changes occurred. HE 1136-2304 remained a Seyfert 1.5 type.

We compared the spectral variations of the data from 1993 to 2017 with the variability behavior in the optical and X-ray continuum. Figure 18 shows the X-ray and optical B-band continuum variations from 2014 to 2016. The long-term trends for 1993–2017 are presented in Figure 19. The *Swift* X-ray data and the ROSAT upper limit for 1990 are presented in red (axis label

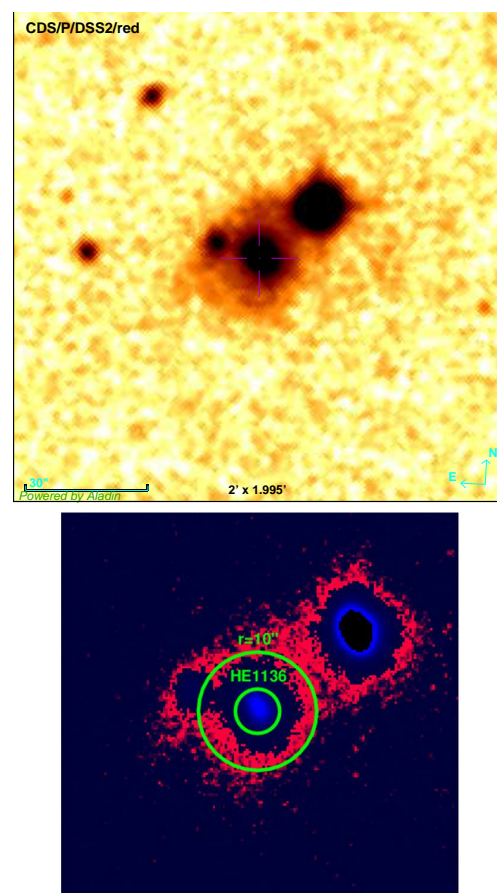


**Fig. 6.** Top: DSS1 image of HE 1136-2304. Scale: 2 x 2 arcmin. North is to the top, East to the left. Bottom: Enlarged B-V two color image based on VYSOS 16 data. The small green circle has  $r = 3.75''$ , indicating that the aperture used for the OCA photometry is sufficiently small to be not contaminated by the star located about  $20''$  in the NW and the faint source in the E. The large green circle with  $r = 10''$  as labeled indicates the projected distance to the eastern source.

on the left side). The optical continuum variations are given in blue.

We scaled the amplitude of the optical light curve with respect to the X-ray light curve. The scaling has been carried out with regard to nearly simultaneous observations in the optical and X-rays in 2014 July and for the combined variability campaign in 2015. The axis label for the blue continuum is given on the right side. Dramatic continuum variations in X-rays and in the optical occurred between 2014 and 2016. The optical continuum closely follows the X-ray flux. HE 1136-2304 was in a low state in X-rays and in the optical before 2000.

#### 4. Discussion

One of the main goals of our optical, UV, and X-ray variability campaign was to investigate the variability behavior of the changing-look AGN HE 1136-2304 subsequent to the outburst in 2014 July. Our campaigns in X-rays and UV, and at optical wavelengths lasted for two and three years, respectively.

A strong and sudden outburst in AGN can in principle be caused by three different events: gravitational lensing, a tidal disruption event (TDE), or major changes in the accretion process. Light curves caused by a lensing effect should exhibit a characteristic smooth, single-peaked shape (e.g., Bruce et al.



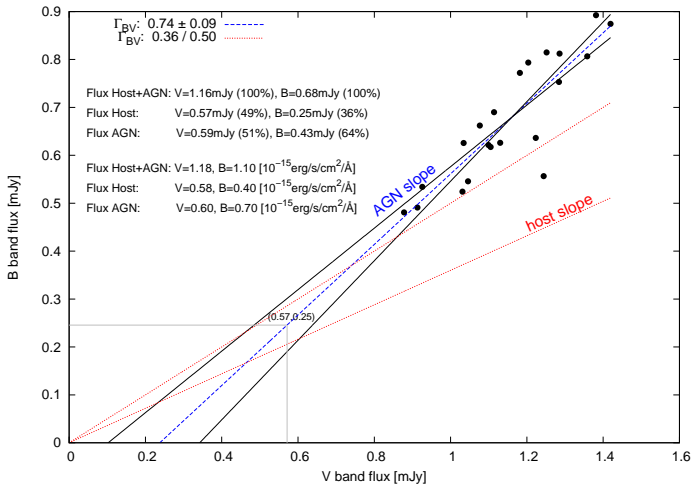


**Fig. 7.** Flux variations (B vs. V) of HE 1136-2304 based on the SALT spectra. The blue dashed line is the best linear fit to the B vs. V fluxes. The black solid lines cover the upper and lower standard deviations of the interpolated AGN slope. The red dashed lines give the range of host slopes as determined by Sakata et al. (2010). The gray lines indicate the central B and V values of the host galaxy. Listed are the B and V flux values (in units of mJy and  $10^{-15} \text{ erg s}^{-1} \text{ cm}^{-2} \text{ \AA}^{-1}$ ) for the combined mean host galaxy+AGN flux, for the host galaxy flux, and for the mean AGN flux.

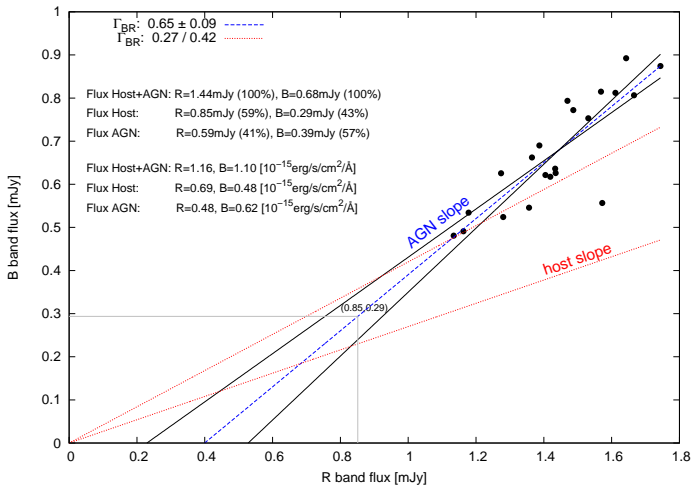


**Fig. 8.** Flux variations (B vs. R) of HE 1136-2304 based on the SALT spectra. The blue dashed line presents the best linear fit to the B vs. R fluxes. The black solid lines cover the upper and lower standard deviations of the interpolated AGN slope. The red dashed lines show the range of host slopes. The gray lines indicate the B and R values of the host galaxy. The B and R flux values are listed as in Fig. 7.

2017). A tidal disruption event is characterized by a sudden dramatic rise in luminosity and a steady decline to quiescence on timescales of months to years (Rees 1988). Some candidates for TDEs in X-rays, UV, and optical bands have been presented by, e.g., Komossa & Bade (1999), Gezari et al. (2008), and Holoien et al. (2016). However, the variability pattern of HE 1136-2304 following the outburst in 2014 shows various outbursts on timescales of days to months typical for “ordinary” AGN variability (see Figures 2, 3, and 4). Therefore, we can rule out a micro lensing or tidal disruption event as the cause of the observed variability pattern seen in HE 1136-2304.

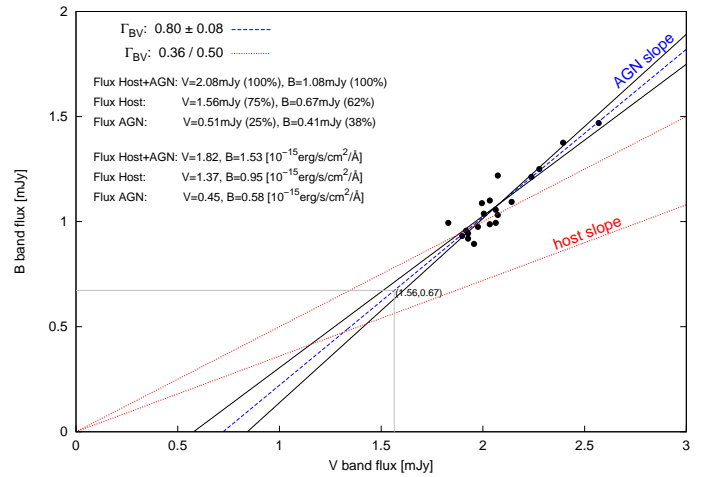


**Fig. 9.** Flux variations (B vs. V) of HE 1136-2304 based on the photometric *Swift* data. The blue dashed line presents the best linear fit to the B vs. V fluxes. The black solid lines cover the upper and lower standard deviations of the interpolated AGN slope. The red dashed lines show the range of host slopes. The gray lines indicate the central B and V values of the host galaxy. The B and V flux values are listed as in Fig. 7.

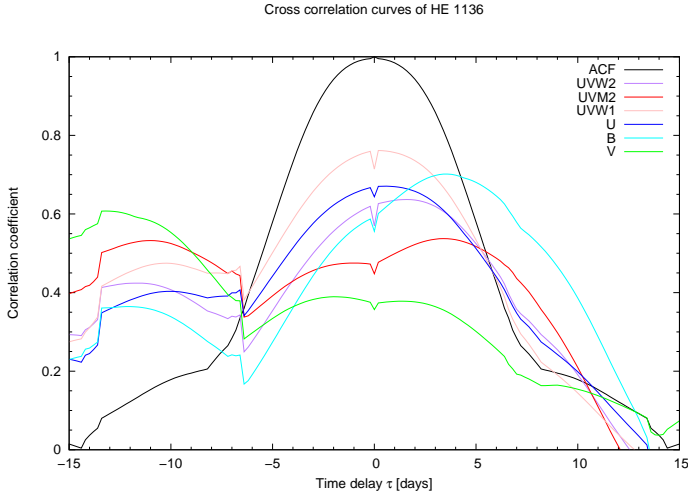
**Table 7.** B, V, and R values (in units of mJy and  $10^{-15} \text{ erg s}^{-1} \text{ cm}^{-2} \text{ \AA}^{-1}$ ) for the combined host galaxy+AGN fluxes as well as for the host galaxy and AGN fluxes alone. These flux values are based on flux variation diagrams in combination with the SALT spectra and with the photometric *Swift* data (see Figs. 7, 8, and 9).

Diagram	B band	V band	R band
(1)	(2)	(3)	(4)
Host+AGN (BvsR SALT)	0.68		1.44
Host+AGN (BvsV SALT)	0.68	1.16	
Host+AGN (BvsV <i>Swift</i> )	1.08	2.08	
Host (BvsR SALT)	0.29		0.85
Host (BvsV SALT)	0.25	0.57	
Host (BvsV <i>Swift</i> )	0.67	1.56	
AGN (BvsR SALT)	0.39		0.59
AGN (BvsV SALT)	0.43	0.59	
AGN (BvsV <i>Swift</i> )	0.41	0.51	
	$[10^{-15} \text{ erg s}^{-1} \text{ cm}^{-2} \text{ \AA}^{-1}]$		
Host+AGN (BvsR SALT)	1.10		1.16
Host+AGN (BvsV SALT)	1.10	1.18	
Host+AGN (BvsV <i>Swift</i> )	1.53	1.82	
Host (BvsR SALT)	0.48		0.69
Host (BvsV SALT)	0.40	0.58	
Host (BvsV <i>Swift</i> )	0.95	1.37	
AGN (BvsR SALT)	0.62		0.48
AGN (BvsV SALT)	0.70	0.60	
AGN (BvsV <i>Swift</i> )	0.58	0.45	

#### 4.1. Optical continuum variability in HE 1136-2304

HE 1136-2304 shows no systematic long-term trends in the continuum light curves (see Figure 2) since the start of our variability campaign in 2014 July. After two years the light curve reaches approximately the same flux level as in 2014 July, while showing unsystematic flux variations down to about 50% in between.

One way to measure the strength of the variability in AGN is to determine their fractional variation  $F_{\text{var}}$ . The fractional vari-



**Fig. 10.** Cross-correlation functions ICCF( $\tau$ ) of the *Swift* bands UVW2, UVM2, UVW1, U, B, and V with respect to the XRT light curve. Also shown is an auto-correlation function (ACF) of the XRT band.

**Table 8.** *Swift* inter-band correlation coefficients ( $r_{max}$ ) and lags ( $\tau$ ).

Band	$r_{max}$	$\tau$ [days]
(1)	(2)	(3)
XRT (ACF)	1.00	0
UVW2	0.64	$1.3^{+3.0}_{-3.5}$
UVM2	0.54	$2.6^{+4.4}_{-4.0}$
UVW1	0.76	$0.3^{+2.9}_{-4.0}$
U	0.67	$0.5^{+3.9}_{-3.0}$
B	0.70	$3.5^{+6.6}_{-2.6}$
V	0.39	—

ation depends on the duration of the monitoring campaign, on the examined wavelength, and on the (accurate) decomposition of the host galaxy contribution. A typical value for the fractional variation  $F_{var}$  of the continuum at  $5100 \text{ \AA}$  is 0.05 to 0.15 for vari-

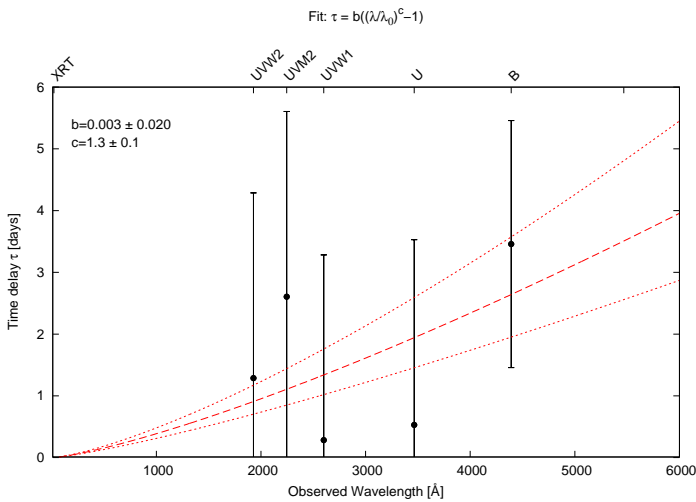


**Fig. 11.** Time delay of the *Swift* UV and optical bands with respect to the *Swift* XRT light curve as a function of the wavelength of the *Swift* bands. The V band has been excluded as it showed a very low correlation coefficient. The dashed line shows the best fit to the data. The dotted lines give the error of the exponent  $c$ .

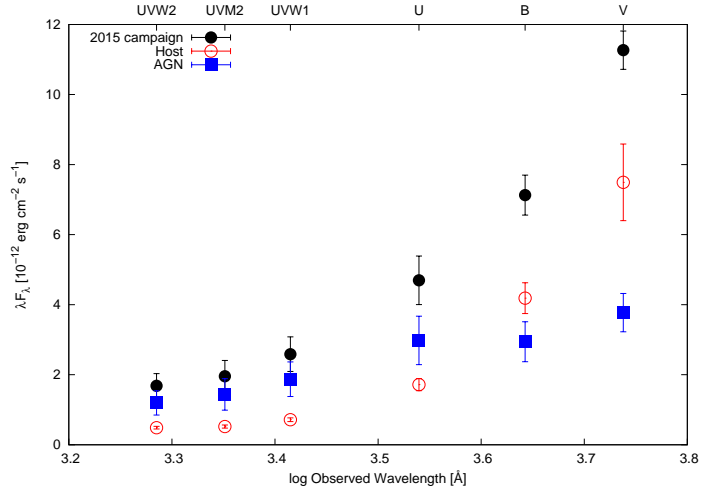


**Fig. 12.** Mean UV and optical spectral energy distribution of HE 1136-2304 based on the *Swift* data taken in 2015 (black filled circles). The red open circles and the blue squares indicate the contributions of the host galaxy and the AGN, respectively.

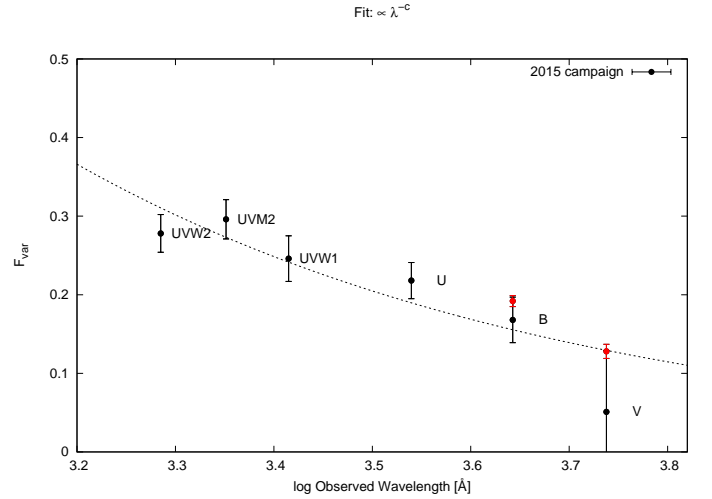


**Fig. 13.** Fractional variations of the UV and optical continuum bands derived from the *Swift* data in 2015 as a function of wavelength. Furthermore, the B and V band measurements based on the photometric data taken in 2015 have been added. The contribution of the host galaxy has been subtracted in all cases. The dashed line shows a general fit with an exponent  $c = 0.84$ .

ability periods of 6–12 months: e.g., NGC 5548 (Peterson et al. 2002, Fausnaugh et al. 2016), 3C 120 (Kollatschny et al. 2014). For variability campaigns over longer periods, typical  $F_{var}$  continuum values at  $5100 \text{ \AA}$  are to 0.1 to 0.25: e.g., NGC 5548 (Peterson et al. 2002), Ark 564 (Shapovalova et al. 2012), Mrk 110 (Kollatschny et al. 2001), or 3C 120 (Kollatschny et al. 2014), and a collection of many AGN in Kollatschny et al. 2006. This higher  $F_{var}$  value is caused by the irregular variations of AGN on longer timescales. There is a higher probability for observing stronger variability amplitudes when monitoring over longer periods of time. We determined optical  $F_{var}$  values of 0.11 ( $5360 \text{ \AA}$ ) and 0.14 ( $4570 \text{ \AA}$ ) for our campaign in 2015 (based on the SALT spectra). Our value of 0.11 for  $F_{var}$  indicates that the continuum variations of HE 1136-2304 were equal to or even stronger than other AGN, in particular after correcting for the flux contribution of the host galaxy.



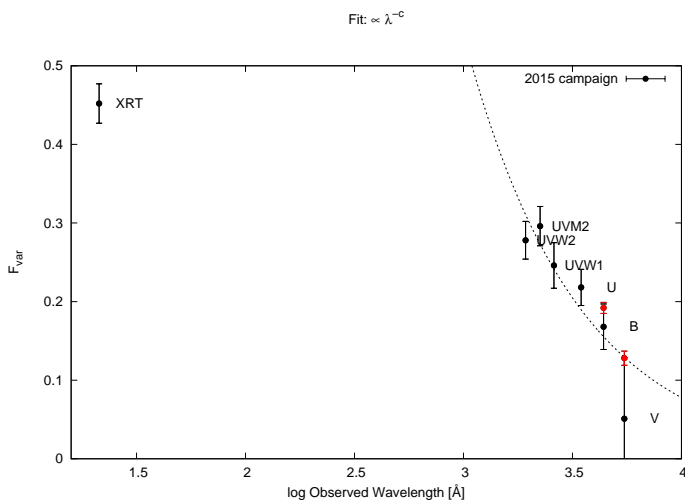


**Fig. 14.** Fractional variations of the X-ray, UV, and optical continuum bands measured from the *Swift* data in 2015 as a function of wavelength.

For a more detailed inspection of the AGN variability, the contribution of the host galaxy starlight should be subtracted before comparing the amplitudes of different AGN. The relative contribution of the host galaxy flux is quite different in spectroscopic and photometric data (see Table 7). The typical contribution of the host galaxy is larger if it is based on broadband photometry because the typical aperture for broadband photometry is larger than that for spectral photometry. One way to estimate the contribution of the host galaxy is to create nucleus-free images of the AGN based on HST images (e.g., Bentz et al. 2009) or by decomposition of the observed AGN spectra (e.g., Barth et al. 2015). Typical values for the relative host galaxy flux contribution are on the order of 20% to 60% in optical AGN spectra (see Figure 4 in Barth et al. 2015). The flux variation gradient (FVG) method (Choloniewski 1981, Winkler et al. 1992, Haas et al. 2011, Ramolla et al. 2015) is another way to estimate the relative contribution of the host galaxy flux to the variable continuum flux. A typical value for the relative contributions of the host galaxy flux is on the order of 50% (e.g., Haas et al. 2011) for broadband photometry. The contribution of the host galaxy flux in HE 1136-2304 amounts to 50% (for spectrum photometry) and to 75% (for broadband photometry) in the V band. Therefore, the variability amplitude in HE 1136-2304 remains quite high in comparison to other AGN after subtraction of the host galaxy flux.

#### 4.2. Comparison of X-ray variations against UV/optical variations

The time delays of the individual *Swift* UV/optical light curves with respect to the *Swift* X-ray light curve are presented in Figure 11. There is a trend that the UV/optical light curves at higher frequencies show shorter delays. A general fit to the data in Figure 11 resulted in a value of  $0.003 \pm 0.020$  light-days for the fit parameter  $b$  in  $\tau = b((\lambda/\lambda_0)^c - 1)$ , with  $\lambda_0 = 25\text{\AA}$ .

This functional form of  $\tau$  has been discussed before by Edelson et al. (2015) and Fausnaugh et al. (2016) in the context of the *Swift* and HST reverberation mapping campaign on NGC 5548. The value of  $b$  gives an estimate of the size of the X-ray emitting region. A value of 0.020 light-days (based on the error of the  $b$  value) corresponds to  $5.1 \times 10^{11}$  m. We can compare this size with the Schwarzschild radius for a central black hole mass of  $M = 4 \times 10^7 M_\odot$  (Kollatschny et al., in prep.):  $1.2 \times 10^{11}$  m. This

indicates that the X-ray emission originates at a distance of a few Schwarzschild radii from the center which is consistent with the last stable orbit of a Schwarzschild black hole.

The second parameter we derived from the general fit shown in Figure 11 is the parameter  $c = 1.3 \pm 0.1$ . This value is close to a theoretically expected value  $c = 1.33 = 4/3$  for an irradiated accretion disk where the geometrically thin, optically thick accretion disk is hotter in the inner radii and cooler in the outer radii (e.g., Cackett et al. 2007, Edelson et al. 2015). The optical continuum is delayed by about three light-days with respect to the X-ray variations. Similar delays of approximately 3 to 4 light-days of the optical continuum bands with respect to the UV/X-ray bands have also been seen in *Swift* variability campaigns of NGC 2617 (Shappee et al. 2014) and NGC 5548 (Fausnaugh et al. 2016). A further indication that the optical continuum in HE 1136-2304 is delayed with respect to the ionizing continuum will be presented in a future paper (Kollatschny et al., in prep.) where we show that the outer line wings, for example in H $\beta$ , respond faster than the adjacent optical continuum.

As shown in Figure 13, the fractional variability  $F_{\text{var}}$  of the continuum bands is a function of their wavelength. The variations are stronger at shorter wavelength bands. This means that the strength of the fractional variability can be considered as a proxy for the distance of the continuum emitting region with respect to the center. Similar to the time delay of the individual continuum bands, we can test whether a power-law model  $F_{\text{var}} = a \cdot \lambda^{-c}$  is consistent with the observations. The optimal  $c$  value  $c = 0.84$  we found is close to a simple power law with  $c = 1$ :  $F_{\text{var}} = a \cdot \lambda^{-1}$ . Furthermore, as shown in Figure 14, the fractional variations in the X-ray band are 50% stronger than those in the UV bands. However, the magnitude of the fractional variation in X-rays is not simply a continuation of the general trend seen in the UV and optical bands. This indicates that the observed X-ray emission does not exactly follow the same trend as the UV/optical emission. The UV/optical continuum emission is generally associated with blackbody emission from the accretion disk (e.g., Hubeny et al. 2001).

We tested whether the observed trend of the fractional variability in the UV/optical bands of HE 1136-2304 is present in other galaxies as well, for example in NGC 5548. An extensive variability campaign of NGC 5548 has been carried out in 2014 (Edelson et al. 2015, Fausnaugh et al. 2016). Their fractional variability data of NGC 5548 are shown in Figure 20. A fit with  $F_{\text{var}} = a \cdot \lambda^{-c}$  and  $c = 0.74$  perfectly matches the observations of NGC 5548. This  $c$  value is close to the optimal  $c$  value of 0.84 we found for HE 1136-2304. A comparison of the fractional variations of NGC 5548 (Figure 20) with those of HE 1136-2304 (Figure 13) shows that the variations in the UV/X-ray bands of HE 1136-2304 are stronger by a factor of 2.3.

However, there are different trends when comparing the variability pattern in X-rays and in the UV/optical observed in HE 1136-2304 with those seen in NGC 5548 (Edelson et al. 2015). The UV/optical light curves of HE 1136-2304 show the same pattern as the X-ray light curve, while this is not the case in NGC 5548 (Edelson et al. 2015). Furthermore, in HE 1136-2304 the strongest variability is observed in X-rays, while this is not the case in NGC 5548. Edelson et al. (2015) suspected that the X-ray flux may not drive the UV/optical light curves in NGC 5548 because of his findings. Such a statement cannot be made for HE 1136-2304 based on its light curves.

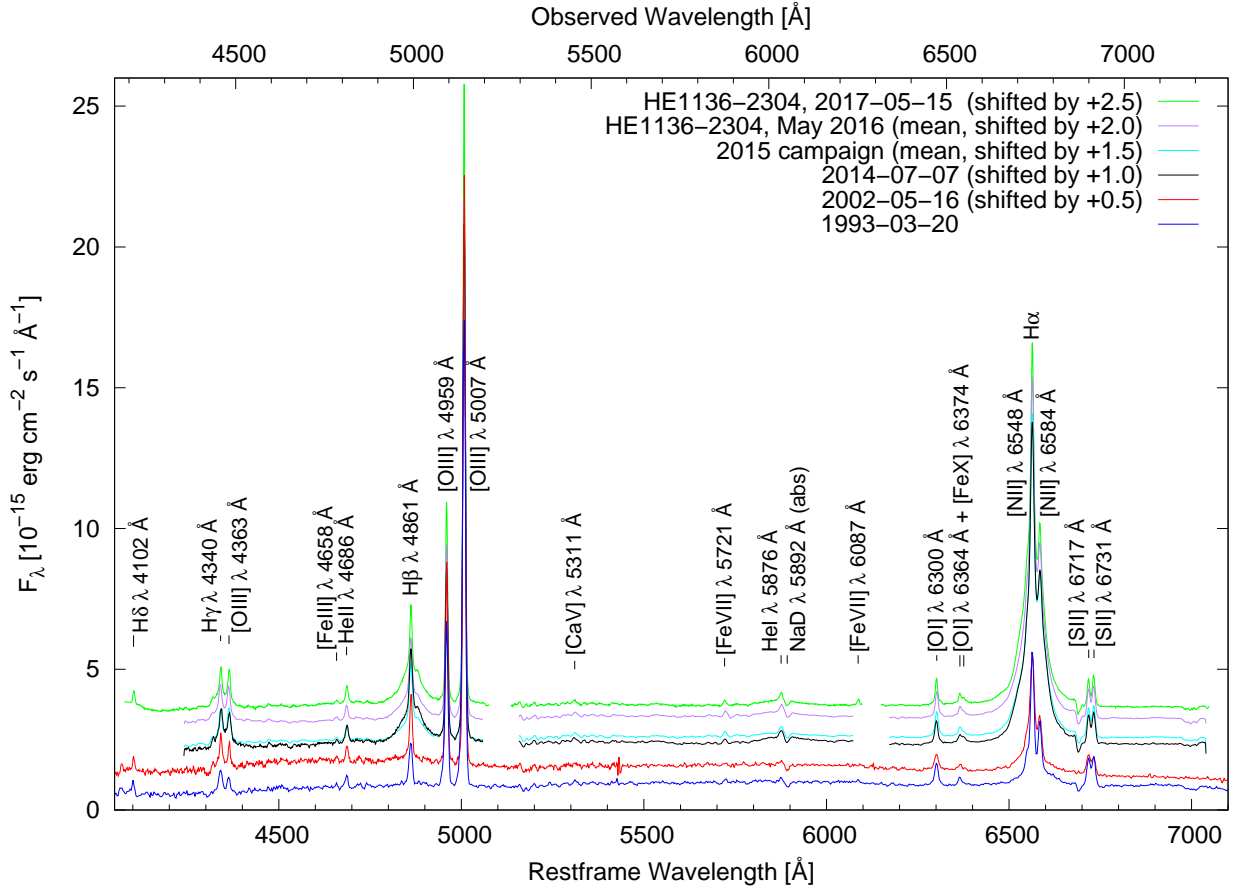


**Fig. 15.** Optical spectra of HE 1136-2304 for the epochs 1993, 2002, 2014, 2017 as well as mean spectra for 2015 and 2016.

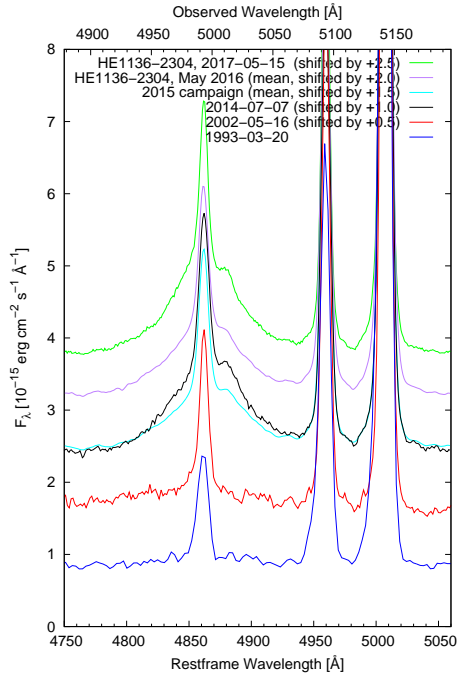


**Fig. 16.** Optical spectra of HE 1136-2304, as in Fig. 15, but showing the H $\beta$  profiles in more detail.

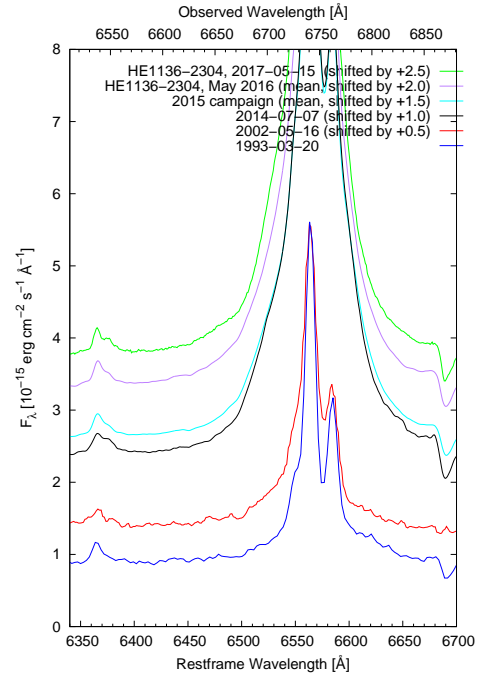


**Fig. 17.** Optical spectra of HE 1136-2304, as in Fig. 15, but showing the H $\alpha$  profiles in more detail.

#### 4.3. Comparison of optical spectral changes with continuum variations in HE 1136-2304

Early optical spectra of HE 1136-2304 were taken in 1993 and 2002. At that time, it was of nearly Seyfert 2 (1.95) type. We

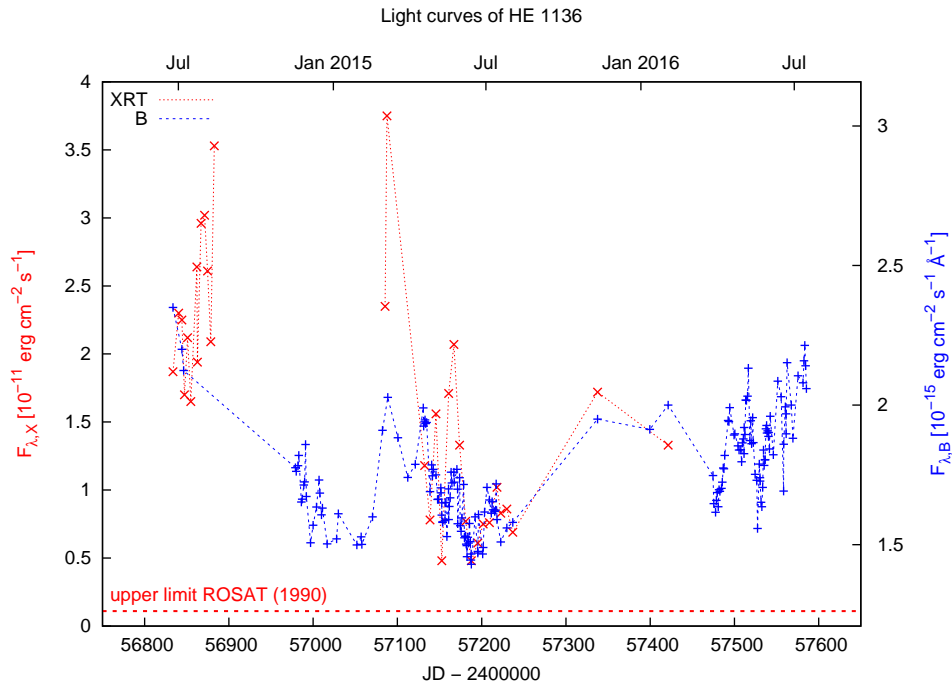


**Fig. 18.** Optical (blue) and X-ray (red) light curve from 2014 to 2016. The upper limit of the X-ray flux in 1990 (ROSAT) is shown by a horizontal dashed line.

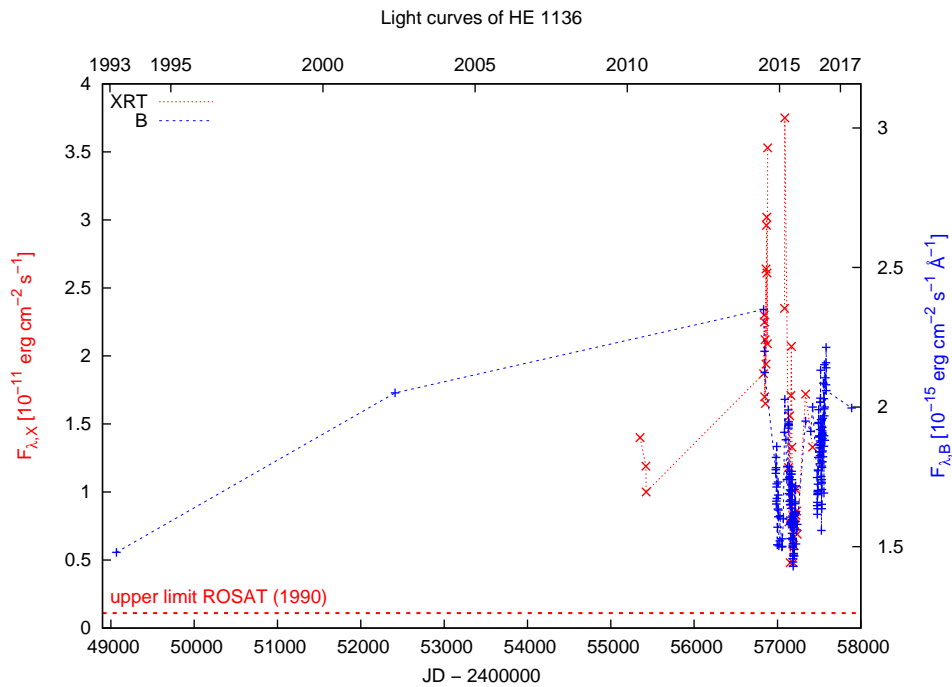


**Fig. 19.** Long-term optical (blue) and X-ray (red) light curves of HE 1136-2304 from 1993–2017. The *Swift* X-ray data and the upper X-ray limit in 1990 based on ROSAT is presented in red (left axis label). The B-band data are scaled with respect to the X-ray data, and are shown in blue (right axis label).

took a spectrum in 2014 July. The spectral type of HE 1136-2304 had changed to be of Seyfert 1.5. Since then the spectral type remained the same (see Figures 15 to 17). There are no major variations present in the Balmer line profiles for the period from 2014 to the present. However, the optical and X-ray continua varied a lot at the same time (see Figure 18).

It has been discussed by Parker et al. (2016) whether the outburst seen in 2014 was caused by a flare due to a stellar disruption event (e.g., Komossa & Bade 1999). In that case we

would have expected a general decline in the continuum flux of HE 1136-2304 over time. However, the observed long-term behavior with repeated phases of decreasing and increasing continuum flux between 2014 and 2017 contradicts this scenario.

On the other hand, Elitzur et al. (2014) present a model in which the broad-line spectral evolution is connected with the AGN luminosity. This might be controlled by the accretion rate onto the central black hole. The long-term variations of HE 1136-2304 from 1993 to 2014 support this model: the X-ray

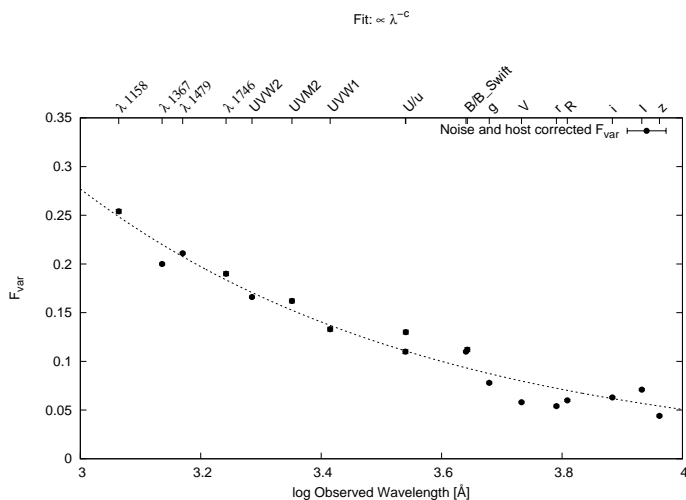


**Fig. 20.** Fit to the fractional variations in the UV and optical bands of an extensive variability campaign of NGC 5548 (with  $c=0.74$ ). The data are from Fausnaugh et al. (2016).

flux increased by a factor of more than ten. The B-band continuum flux (without correction for the host galaxy contribution) increased by more than 60%, and the spectral type changed from a nearly Seyfert 2 type to a Seyfert 1.5 type. A similar scenario, but with decreasing continuum flux, has been found for Fairall 9. The continuum flux dropped to 20% of its original flux in 1978, and its spectral type changed from a quasar/Seyfert 1 type to a Seyfert 1.95 type within six years (Kollatschny & Fricke, 1985). Spectral variations of this kind generally occur on timescales of years.

However, the spectral type variations seem not to follow the continuum intensity variations on shorter timescales (weeks to months). In 2015, HE 1136-2304 varied in the X-rays by a factor of eight within two months (see Figure 18), whereas the broad-line profiles varied only marginally over the period from 2014 to 2017 (see Figure 15). A detailed discussion of the spectral variability campaign carried out in 2015 will be presented in a separate paper (Kollatschny et al., in prep.).

## 5. Summary

We present results of an optical, UV, and X-ray monitoring campaign of the changing-look AGN HE 1136-2304 carried out from 2014 to 2017. This campaign took place after a continuum outburst in the optical and X-rays in 2014 July connected to a spectral change from a Seyfert 1.95 to a Seyfert 1.5 type. Our findings can be summarized as follows:

- (1) The optical, UV, and X-ray continuum light curves show the same variability pattern. The amplitude decreases with increasing wavelength. It varies by a factor of eight in X-rays, by a factor of four in the UV, and by a factor of two in the optical continuum between 2014 and 2016. The amplitude in the optical increases by a factor of three after correction for the host galaxy contribution.
- (2) No general trend was visible in the variability pattern. This rules out that the outburst in 2014 was caused by gravitational lensing or by a tidal disruption event. In these cases we would have expected a general decrease in the emitted continuum flux.
- (3) The optical B-band continuum light curve is delayed by about three days with respect to the X-ray light curve.

- (4) The spectral type of HE 1136-2304 remained as Seyfert 1.5 between 2014 and 2017 despite its strong continuum variations at the same time.

*Acknowledgements.* We are thankful to the late Neil Gehrels for approving our ToO requests. We also thank the *Swift* team for performing the ToO observations. This research has made use of the XRT Data Analysis Software (XRTDAS) developed under the responsibility of the ASI Science Data Center (ASDC), Italy. This research has made use of the NASA/IPAC Extragalactic Database (NED) which is operated by the Jet Propulsion Laboratory, Caltech, under contract with the National Aeronautics and Space Administration. This work has been supported by the DFG grants Ha 3555/12-1, Ko 857/32-2 and Ko 857/33-1.

## References

- Arnaud, K. A., 1996, ASP Conf. Ser. 101: Astronomical Data Analysis Software and Systems V, 101, 17
- Barth, A.J., et al. 2015, ApJS, 217, 26
- Bentz, M.C., et al. 2009, ApJ, 697, 160
- Breeveld, A.A., et al. 2010, MNRAS, 406, 1687
- Bruce, A., et al. 2017, MNRAS, 467, 1259
- Burrows, D., et al. 2005, Space Science Reviews, 120, 165
- Cackett, E.M., Horne, K., & Winkler, H. 2007, MNRAS, 380, 669
- Cardelli, J.A., Clayton, G.C., Mathis, J.S., 1989, ApJ, 345, 245
- Collin-Souffrin, S., et al. 1973, A&A, 22, 343
- Cash, W., 1979, ApJ, 228, 939
- Choloniewski, J., 1981, Acta Astron., 31, 293
- Denney, K.D., et al. 2014, ApJ, 796, 134
- Dietrich, M., Kollatschny, W. 1995, A&A, 303, 405
- Edelson, R., et al. 2002, ApJ, 568, 610
- Edelson, R., et al. 2015, ApJ, 806, 129
- Elitzur, M., Ho, L.C., Trump, J.R. 2014, MNRAS, 438, 3340
- Fausnaugh, M.M. et al. 2016, ApJ, 821, 56
- Fitzpatrick, E.L. 1999, PASP, 111, 63
- Gehrels, N., et al. 2004, ApJ, 611, 1005
- Gezari, S. et al. 2008, ApJ, 676, 944
- Grupe, D., Thomas, H.-C., & Beuermann, K., 2001, A&A, 367, 470
- Grupe, D., Komossa, S., Leighly, K.M., & Page, K.L., 2010, ApJS, 187,64
- Guainazzi, M. 2002, MNRAS, 329, L13
- Haas, M., et al. 2011, A&A, 535, 73
- Hill, J.E., et al. 2004, SPIE, 5165, 217
- Holoien, T. W.-S. et al. 2016, MNRAS, 455, 2918
- Hubeny, I. et al. 2001, ApJ, 559, 680
- Jones, D.H., et al. 2004, MNRAS, 355, 747
- Kabath, P., et al. 2009, A&A, 506, 569
- Kalberla, P.M.W., Burton, W.B., Hartmann, D., et al. A&A, 440, 775
- Kinney, A.L. et al. 1996, ApJ, 467, 38
- Kollatschny, W. 2003, A&A, 407, 461
- Kollatschny, W., Bischoff, K., Dietrich, M. 2000, A&A, 361, 901
- Kollatschny, W., Bischoff, K., Robinson, E. L., et al. 2001, A&A, 379, 125
- Kollatschny, W., & Fricke, K.J., 1985, A&A, 146, L11
- Kollatschny, W., et al. 2014, A&A, 566, 36
- Kollatschny, W., & Zetzl, M. 2006, A&A, 454, 459
- Kollatschny, W., & Zetzl, M. 2010, A&A, 522, 36
- Komossa, S., et al. 2008, ApJ, 678, L13
- Komossa, S., Bade, N. 1999, A&A, 343, 775
- LaMassa, S.M., et al. 2015, ApJ, 800, 144
- Landolt, A. U. 2009, AJ, 137, 4186
- Macleod, C. L., et al. 2016, MNRAS, 457, 389
- Patat, F., et al. 2011, A&AS27, 91
- Park, T., Kashyap, V.L., Siemiginowska, A., van Dyk, D.A., Zezas, A., Heinke, C., & Wargelin, B.J., 2006, ApJ, 652, 610
- Parker, M. L., Komossa, S., Kollatschny, W., et al. 2016, MNRAS, 461, 1927
- Pei, L., et al. 2017, ApJ, 837, 131
- Penston, M. V., & Perez, E. 1984, MNRAS, 211, 33
- Peterson, B.M., Wanders, I., Bertram, R., et al. 1998, ApJ, 501, 82
- Peterson, B.M., et al. 2002, ApJ, 581, 197
- Peterson, B.M., et al. 2004, ApJ, 613, 682
- Poole, T.S. et al. 2008, MNRAS, 383, 627
- Pozo Nunez, F., et al. 2015, A&A, 576, 73
- Ramolla, M., et al. 2013, AN, 334, 1115
- Ramolla, M., et al. 2015, A&A, 581, 93
- Rees, M. 1988, Nature, 333, 523
- Reimers, D., et al. 1996, A&AS, 115, 235
- Rodríguez-Pascual P.M., Alloin D., Clavel J., et al. 1997, ApJS 110, 9
- Roming, P.W.A., et al. 2005, Space Science Reviews, 120, 95
- Roming, P.W.A., et al. 2009, ApJ, 690, 163
- Runnoe, J.C. et al. 2016, MNRAS, 455, 1691
- Sakata Y., et al. 2010, ApJ 711, 461
- Schlafly E.F., & Finkbeiner, 2011, ApJ 737, 103
- Schlegel D.J., et al. 1998, ApJ 500, 525
- Shapovalova, A.I., et al. 2010, A&A, 517, 42
- Shapovalova, A.I., et al. 2012, ApJS, 201, 10
- Shappee, B.J., et al. 2014, ApJ, 788, 48
- Winkler, H. et al. 1992, MNRAS, 257, 659
- Wright, E.L., 2006, PASP, 118, 1711

**Appendix A: Additional tables**

**Table A.1.** XRT and UVOT monitoring observation log: Julian date, UT Date, and XRT and UVOT exposure times in seconds.

Julian Date 2 400 000+	UT Date	XRT	V	B	U	UV W1	UV M2	UVW2
55350.7604	2010-06-03 06:15	3828	—	—	—	—	3805	—
55420.4688	2010-08-11 23:15	1643	—	—	—	1639	—	—
55424.4167	2010-08-15 23:00	3685	—	—	—	2665	—	—
56833.6090	2014-06-25 02:45	1573	130	130	130	260	380	520
56840.3437	2014-07-01 20:15	1021	—	—	—	—	—	1018
56844.1424	2014-07-05 15:25	1019	83	83	83	166	246	333
56847.2729	2014-07-08 18:33	979	—	—	—	—	979	—
56850.9375	2014-07-12 10:30	1039	—	—	—	—	1025	—
56854.8646	2014-07-16 08:10	817	—	—	—	—	820	—
56861.9479	2014-07-23 10:43	1051	—	—	—	—	1060	—
56862.6007	2014-07-24 02:26	724	—	—	—	—	735	—
56866.9965	2014-07-28 11:53	949	—	—	—	—	936	—
56871.0729	2014-08-01 13:46	998	—	—	—	—	756	—
56874.1007	2014-08-05 02:25	948	—	—	—	—	946	—
56878.5347	2014-08-09 00:49	599	—	—	—	—	592	—
56882.7340	2014-08-13 05:38	1017	—	—	—	—	1008	—
57085.3507	2015-03-03 20:23	957	—	—	952	—	—	—
57087.5208	2015-03-06 00:31	826	—	—	—	828	—	—
57132.3125	2015-04-19 19:35	1186	95	95	95	190	267	381
57138.7500	2015-04-26 06:00	1892	153	153	153	306	451	613
57145.8368	2015-05-03 08:05	1326	109	109	106	216	297	438
57152.6875	2015-05-10 04:10	2253	182	182	182	365	100	730
57160.9028	2015-05-18 09:39	587	52	52	52	103	114	207
57167.0833	2015-05-24 14:00	2208	182	182	182	365	494	734
57173.8160	2015-05-31 07:25	1436	116	116	116	233	331	466
57181.0000	2015-06-07 12:00	2662	216	216	216	432	623	866
57187.8056	2015-06-14 07:20	2003	164	164	164	326	465	654
57194.9236	2015-06-21 22:30	1888	154	154	154	310	430	618
57201.8785	2015-06-28 09:03	1521	126	126	126	251	366	503
57209.3986	2015-07-05 21:34	2597	205	205	205	414	616	827
57218.2188	2015-07-14 17:15	2138	175	175	175	350	481	701
57222.6285	2015-07-19 03:05	2165	172	172	172	346	515	692
57229.9167	2015-07-26 09:55	1963	159	159	159	317	472	636
57236.9687	2015-08-02 11:17	1955	158	158	158	316	480	632
57337.5763	2015-11-11 01:50	1983	161	161	161	321	482	642
57421.3507	2016-02-02 20:25	1963	157	157	157	314	472	630

**Table A.2.** Log of photometric observations with MONET/North (N) and MONET/South (S): Julian date, UT date, used filters, and telescope.

Julian Date 2 400 000+	UT Date	Filter	Telescope
56979.010	2014-11-17	B, V, R	N
56979.968	2014-11-18	B, V, R	N
56981.980	2014-11-20	B, V, R	N
56982.971	2014-11-21	B, V, R	N
56985.947	2014-11-24	B, V, R	N
56986.936	2014-11-25	B, V, R	N
56988.945	2014-11-27	B, V, R	N
56989.936	2014-11-28	B, V, R	N
56991.034	2014-11-29	B, V, R	N
56991.987	2014-11-30	B, V, R	N
56996.924	2014-12-05	B, V, R	N
56997.921	2014-12-06	B, V, R	N
56999.890	2014-12-08	B, V, R	N
57004.007	2014-12-12	B, V, R	N
57006.928	2014-12-15	B, V, R	N
57008.023	2014-12-16	B, V, R	N
57009.928	2014-12-18	B, V, R	N
57011.018	2014-12-19	B, V, R	N
57027.909	2015-01-05	B, V, R	N
57029.911	2015-01-07	B, V, R	N
57051.844	2015-01-29	B, V, R	N
57056.946	2015-02-03	B, V, R	N
57057.827	2015-02-04	B, V, R	N
57504.252	2016-04-25	B, V, R	S
57505.513	2016-04-26	B, V, R	S
57511.399	2016-05-02	B, R	S
57513.282	2016-05-04	B, V	S
57514.333	2016-05-05	B, V	S
57518.273	2016-05-09	B, V, R	S
57520.353	2016-05-11	B, V, R	S
57530.295	2016-05-21	B, V, R	S
57535.293	2016-05-26	B, V, R	S
57536.314	2016-05-27	B, V, R	S
57537.309	2016-05-28	B, V, R	S
57538.230	2016-05-29	B, V, R	S
57546.234	2016-06-06	B, V, R	S
57558.358	2016-06-18	B, V, R	S
57561.329	2016-06-21	B, V, R	S

**Table A.3.** Log of photometric observations with VYSOS 16 (V 16) and BEST II (B II): Julian date, used filter, and telescope.

Julian Date 2 400 000+	Filter	Telescope	Julian Date 2 400 000+	Filter	Telescope
57130.705	B, V, NB <sub>670</sub>	V 16	57203.486	B	B II
57132.680	B, V, NB <sub>670</sub>	V 16	57211.467	NB <sub>670</sub>	V 16
57133.627	B, V, NB <sub>670</sub>	V 16	57211.488	B	B II
57134.649	B, V, NB <sub>670</sub>	V 16	57212.468	NB <sub>670</sub>	V 16
57140.622	B, V, NB <sub>670</sub>	V 16	57212.488	B	B II
57141.572	B, V, NB <sub>670</sub>	V 16	57213.491	B	B II
57142.571	B, V, NB <sub>670</sub>	V 16	57215.465	NB <sub>670</sub>	V 16
57143.696	NB <sub>670</sub>	V 16	57215.489	B	B II
57144.670	NB <sub>670</sub>	V 16	57216.488	NB <sub>670</sub>	V 16
57145.621	NB <sub>670</sub>	V 16	57216.519	B	B II
57145.670	V	V 16	57219.465	NB <sub>670</sub>	V 16
57146.695	NB <sub>670</sub>	V 16	57220.465	NB <sub>670</sub>	V 16
57147.620	NB <sub>670</sub>	V 16	57221.465	NB <sub>670</sub>	V 16
57147.651	B	V 16	57229.468	NB <sub>670</sub>	V 16
57148.656	B, V, NB <sub>670</sub>	V 16	57230.468	NB <sub>670</sub>	V 16
57150.644	V	V 16	57231.468	NB <sub>670</sub>	V 16
57151.581	B, V, NB <sub>670</sub>	V 16	57474.588	V	V16
57151.663	B	B II	57475.558	B, V, NB <sub>670</sub>	V16
57152.727	B	B II	57477.599	B, V, NB <sub>670</sub>	V16
57153.585	B, V, NB <sub>670</sub>	V 16	57478.581	B, V, NB <sub>670</sub>	V16
57153.636	B	B II	57479.555	B, V, NB <sub>670</sub>	V16
57156.555	B, V, NB <sub>670</sub>	V 16	57480.747	B, V, NB <sub>670</sub>	V16
57156.667	B	B II	57481.686	B, V, NB <sub>670</sub>	V16
57157.556	V, NB <sub>670</sub>	V 16	57482.737	B, V, NB <sub>670</sub>	V16
57157.663	B	B II	57484.606	B, V, NB <sub>670</sub>	V16
57158.653	V, NB <sub>670</sub>	V 16	57485.552	B, V, NB <sub>670</sub>	V16
57158.735	B	B II	57486.667	B, V, NB <sub>670</sub>	V16
57160.600	NB <sub>670</sub>	V 16	57492.493	B, V, NB <sub>670</sub>	V16
57160.681	B	B II	57493.515	B, V, NB <sub>670</sub>	V16
57161.555	V, NB <sub>670</sub>	V 16	57494.495	B, V, NB <sub>670</sub>	V16
57161.637	B	B II	57499.489	B, V, NB <sub>670</sub>	V16
57162.606	V, NB <sub>670</sub>	V 16	57500.488	B, V, NB <sub>670</sub>	V16
57162.639	B	B II	57507.599	B, V, NB <sub>670</sub>	V16
57163.553	V, NB <sub>670</sub>	V 16	57508.497	B, V, NB <sub>670</sub>	V16
57163.722	B	B II	57509.484	B, V, NB <sub>670</sub>	V16
57164.553	V, NB <sub>670</sub>	V 16	57510.565	B, V, NB <sub>670</sub>	V16
57164.639	B	B II	57511.530	B, V, NB <sub>670</sub>	V16
57165.658	V	V 16	57512.489	B, V, NB <sub>670</sub>	V16
57169.598	V, NB <sub>670</sub>	V 16	57515.553	B, V, NB <sub>670</sub>	V16
57170.533	V, NB <sub>670</sub>	V 16	57516.517	B, V, NB <sub>670</sub>	V16
57170.546	B	B II	57521.629	B, V, NB <sub>670</sub>	V16
57171.554	V, NB <sub>670</sub>	V 16	57522.461	B, V, NB <sub>670</sub>	V16
57171.601	B	B II	57524.471	B, V, NB <sub>670</sub>	V16
57174.586	V, NB <sub>670</sub>	V 16	57526.462	B, V, NB <sub>670</sub>	V16
57174.628	B	B II	57527.460	B, NB <sub>670</sub>	V16
57175.553	V, NB <sub>670</sub>	V 16	57529.463	B, NB <sub>670</sub>	V16
57175.595	B	B II	57530.459	B	V16
57176.558	V, NB <sub>670</sub>	V 16	57531.639	B, NB <sub>670</sub>	V16
57176.595	B	B II	57532.509	B, NB <sub>670</sub>	V16
57177.614	V	V 16	57533.458	B, NB <sub>670</sub>	V16
57178.566	V, NB <sub>670</sub>	V 16	57534.519	B, NB <sub>670</sub>	V16
57178.595	B	B II	57536.458	B, NB <sub>670</sub>	V16
57179.552	V, NB <sub>670</sub>	V 16	57538.626	B, NB <sub>670</sub>	V16
57179.595	B	B II	57539.487	B	V16
57180.568	V, NB <sub>670</sub>	V 16	57540.599	B, NB <sub>670</sub>	V16
57180.596	B	B II	57541.542	B, NB <sub>670</sub>	V16
57181.552	V, NB <sub>670</sub>	V 16	57542.536	B, NB <sub>670</sub>	V16
57181.596	B	B II	57551.512	B, NB <sub>670</sub>	V16
57182.553	V, NB <sub>670</sub>	V 16	57555.463	B, NB <sub>670</sub>	V16
57182.600	B	B II	57558.459	B, NB <sub>670</sub>	V16



Table A.3. continued.

Julian Date 2 400 000+	Filter	Telescope	Julian Date 2 400 000+	Filter	Telescope
57183.515	V, NB <sub>670</sub>	V 16	57560.459	B, NB <sub>670</sub>	V16
57183.570	B	B II	57561.463	B, NB <sub>670</sub>	V16
57184.515	V, NB <sub>670</sub>	V 16	57562.459	B, NB <sub>670</sub>	V16
57184.569	B	B II	57567.460	B, NB <sub>670</sub>	V16
57185.515	V, NB <sub>670</sub>	V 16	57569.461	B, V, NB <sub>670</sub>	V16
57185.569	B	B II	57575.467	B, V, NB <sub>670</sub>	V16
57186.515	V, NB <sub>670</sub>	V 16	57581.468	B, V, NB <sub>670</sub>	V16
57186.570	B	B II	57582.469	B, NB <sub>670</sub>	V16
57187.516	V, NB <sub>670</sub>	V 16	57583.468	B, NB <sub>670</sub>	V16
57187.570	B	B II	57584.464	B, NB <sub>670</sub>	V16
57189.516	V, NB <sub>670</sub>	V 16	57585.504	B, NB <sub>670</sub>	V16
57192.518	V, NB <sub>670</sub>	V 16	57473.593	B	V16
57195.497	V, NB <sub>670</sub>	V 16	57474.570	NB <sub>670</sub>	V16
57195.510	B	B II	57475.540	NB <sub>670</sub>	V16
57198.497	V, NB <sub>670</sub>	V 16	57477.581	NB <sub>670</sub>	V16
57203.461	V, NB <sub>670</sub>	V 16	57478.563	NB <sub>670</sub>	V16